Published in final edited form as:
Clin Chest Med. 2008 March ; 29(1): 195–vii. doi:10.1016/j.ccm.2007.12.003.

Functional Imaging: CT and MRI

Edwin JR van Beek, MD and **Eric A Hoffman, PhD**
Department of Radiology, Carver College of Medicine, University of Iowa, Iowa City, USA

Abstract

Synopsis—Numerous imaging techniques permit evaluation of regional pulmonary function. Contrast-enhanced CT methods now allow assessment of vasculature and lung perfusion. Techniques using spirometric controlled MDCT allow for quantification of presence and distribution of parenchymal and airway pathology, Xenon gas can be employed to assess regional ventilation of the lungs and rapid bolus injections of iodinated contrast agent can provide quantitative measure of regional parenchymal perfusion. Advances in magnetic resonance imaging (MRI) of the lung include gadolinium-enhanced perfusion imaging and hyperpolarized helium imaging, which can allow imaging of pulmonary ventilation and .measurement of the size of emphysematous spaces.

Keywords

Quantitative CT; Airways; Parenchyma; Ventilation; Perfusion; Xenon CT; Computer Aided Detection; Lung Function; MDCT; MRI; Dual Source CT

INTRODUCTION

The traditional approach to lung imaging, using so-called high-resolution computed tomography (HRCT) consisting of 1 mm slices, is increasingly replaced by novel methods. The introduction of multi-detector row CT (MDCT) has enabled coronal, sagital, and oblique reformatting at greater spatial resolution than before, while contrast-enhanced CT methods now allow assessment of vasculature and lung perfusion. Developments do not stop there: techniques using spirometric controlled MDCT allow for quantification of presence and distribution of parenchymal and airway pathology, Xenon gas can be employed to assess regional ventilation of the lungs; and, although many such applications are currently still driven by research, it is expected that HRCT will become antiquated in the not too distant future as CT evolves from mere static assessment of morphology into a dynamic and quantifiable tool for regional assessment of the lung.

Complementary to CT of the lung, magnetic resonance imaging (MRI) of the lung, which previously was handicapped by field inhomogeneity and the lack of protons in lung tissue, is developing its own arsenal for lung assessment, both in terms of morphology, pulmonary circulation, ventilation, and right heart assessment. It is clear that the inherent advantage of MRI over CT – its lack of ionizing radiation – makes it of primary interest in the field of lung

Correspondence: Edwin JR van Beek MD PhD FRCR, Department of Radiology, Carver College of Medicine, University of Iowa, C-751 GH, 200 Hawkins Drive, Iowa City, IA 52242-1077, USA, tel 319-384-6133, FAX 319-356-1503, e-mail: edwin-vanbeek@uiowa.edu, Eric A. Hoffman, PhD, Department of Radiology, Carver College of Medicine, University of Iowa, C-751 GH, 200 Hawkins Drive, Iowa City, IA 52242-1077, USA, tel 319-356-1381, FAX 319-356-1503, e-mail: eric-hoffman@uiowa.edu.

diseases which tend to be chronic with acute exacerbations, thus requiring multiple investigations during the life-span of the patient. Unfortunately, availability of some of the tools required such as gas polarizers, or MRI techniques such as broadband upgrades, is still somewhat limited. However, there is a significant drive towards making access easier and in many centers MRI has already become a main diagnostic tool.

This chapter intends to describe some of the new features involving lung imaging, both from a CT and a MRI perspective. It is our intention that the reader be familiar with the currently available techniques as well as those that are expected to reach clinical applications in the near future.

COMPUTED TOMOGRAPHY

The scanners

Volumetric physiological imaging via x-ray CT had its beginning in the mid 1970's with the Dynamic Spatial Reconstructor, the prototype of dynamic volumetric X-ray CT designed and installed at the Mayo Clinic (1). Much of the work establishing the accuracy and precision of volumetric lung imaging was performed on the DSR. (1,2). The primary lesson learned from the DSR was that lungs in particular must be studied dynamically and volumetrically. Commercial imaging technology lagged significantly behind this early work. The electron beam CT (EBCT), (3) used parallel X-ray targets to get improved scan speeds up to 50 msec per slice pair, acquiring eight stacked slices in approximately 224 milliseconds. There have been rapid advances in speed and resolution with the advent of MDCT (4). Its cone-beam spiral CT uses a 2D detector array, allowing larger scanning range in shorter time with higher image resolution (5,6). Acquiring multiple image slices per rotation with rotation speeds as short as 0.3sec allows for a significant reduction in acquisition time. Faster scan times will significantly impact functional imaging protocols where the rate of perfusion of a contrast agent is measured over time or gated imaging is needed. We have believed the future of lung assessment resides with true dynamic low dose volumetric CT scanners that image at least 1/3 of the thorax with at least a 0.5mm isotropic voxel and achieve a full rotation scan aperture of 150 msec and have superior contrast resolution for radiopaque gas and injected contrast detection. The system will be likely coupled with a low Tesla MR scanner which will be used to complement the information available from the CT image. Patients will be scanned frequently by low tesla MR and less frequently over time by use of the CT component.

With the introduction of dual source MDCT (7,8)into the clinical arena, scan apertures now fall below 150 msec, but z axis coverage with single rotation on these scanners remains at 2.4cm. Other single source spiral scanners have advanced to as many as 256 rows of detectors (9,10) with a z-axis coverage of up to 12cm. By the end of 2007, 128 rows and 4cm z-axis coverage will be the minimum configuration of the high-end MDCT scanners. With the broader coverage, retrospective gating methods have emerged for both cardiac as well as pulmonary imaging whereby, via a very low pitch, images are gathered during the respiratory or cardiac cycles while recording the physiologic signal together with the projection images. Prospectively, (11) or retrospectively(10,12–17), the portions of the physiologic cycle of interest can be selected from within the slow pitch spiral data such that a volumetric image data set is reconstructed for just that location of the respiratory or cardiac cycle. Multiple portions of the physiologic cycle can thus be reconstructed to yield a dynamic image sequence of the organ of interest. (10,12–17) In pulmonary applications, the earliest use of this method has been in oncology, tracking the maximum trajectory throughout a respiratory cycle for the purposes of treatment planning. (15,18).

As the scanners become faster with more slices, some have questioned how many slices is enough. The answer to this question is largely determined by the more advanced functional

applications such as retrospective gating technologies, ventilation, and/or perfusion imaging. As discussed below, perfusion and ventilation imaging requires an axial mode of scanning to dynamically track the first pass of a sharp bolus of contrast agent (approximately 0.5cc/kg over 2–3 seconds injected into the vena cava/right atrial junction). With axial dynamic scanning, the functional parameter under investigation (ventilation or perfusion in the case of the lung) is evaluated only as broadly along the z-axis as the coverage of the multiple rows of detectors will permit (typically 4–12 cm). If it is important to dynamically evaluate the whole lung then one must have a long z-axis coverage: otherwise the dynamic acquisition will have to be repeated at multiple levels to gain the z-axis coverage. There must be enough rows of detectors to maintain structural detail as well as apex-to-base coverage.

With the introduction of dual source CT, there is a growing interest in the use of dual energy (19–22) as a means of characterizing tissues regionally as well as quantitating local amounts of a contrast agent. Dual energy imaging permits mathematical separation of the contrast signal from the background tissue signal on a single scan acquisition, without the. This simultaneous acquisition avoids the need for acquisition of separate unenhanced and enhanced scans, with associated of added radiation dose, and alignment challenges due to variations in breath hold, cardiogenic motion, alterations in chest wall configuration during a breath hold, normal stress relaxation occurring when the lung is held at a fixed inflation pressure, etc.. In the case of a perfused blood volume scan used to assess pulmonary emboli, it is possible, through the use of dual energy whereby one x-ray source is set to 80kV and the other to 140kV, to generate a virtual contrast-only image as well as a virtual unenhanced image(20). The accuracy of the Hounsfield units in the virtual unenhanced image remains untested, and thus it is not clear whether this virtual image data set can be used, for instance, in a density mask analysis seeking to quantify presence and distribution of emphysema in a smoker being imaged with a contrast enhanced scan for the detection and characterization of lung nodules.

With the growing use of prolonged infusions of iodinated x-ray contrast agent, to detect pulmonary emboli, the enhancement has been used as an index of regional pulmonary blood flow. This has been and should be dubbed as a “perfused blood volume“ scan, (23–25) so as not to confuse this measure with the quantitative assessment of parenchymal perfusion discussed below. With dual energy imaging, it may be possible to obtain a volumetric image of regional ventilation along with regional lung structure by imaging with dual energy spiral scanning during a single breath of xenon gas . (21,22) This again is an experimental method yet to be validated against the dynamic xenon CT assessment of regional ventilation discussed later in this section. The single breath, dual energy xenon method has been successfully employed in rabbits using a synchrotron source. (26–28)

Quantitative image analysis

Critical to taking full advantage of MDCT (and MRI) is the ability to objectively evaluate the information content of the images. In the case of the lung, the starting point is reliable detection of the lungs (29), lobes (30), airways (31–41) , and blood vessels followed by an analysis of parenchymal attenuation and texture and finally a regional quantification of ventilation and perfusion parameters. We and others have reviewed these capabilities elsewhere (42,43). With the advent of MDCT and isotropic voxels, it is now possible to reliably segment the airway tree to approximately the 5^{th} generation (trachea being generation 0) and many of the 6^{th} and 7^{th} generation branches are captured in the segmentation. Airway wall thickness is commonly expressed as wall area percent (percent of the area defined by the outer wall of the airway segment occupied by the airway wall). (44). These measures are being used to assess airway remodeling in both asthma and COPD. Figure 1 shows a depiction of the airway tree and lobe segmentation from both a normal non-smoker and a patient with COPD. These images can be used to not only quantify the airway and parenchyma characteristics but also to provide a

roadmap linking airway paths to sub-lobar segment. These data were acquired using the VIDA PW+ workstation (Coralville, Iowa).

Evaluation of the lung at its functional interface

Computer-based methods for objective quantitation of MDCT data sets to compare normal and diseased lung are increasingly being used in conjunction with 2D data sets. Methods have ranged from counting the number of voxels below a cut-off (−850, −910, −950HU) (45–56) to those which make use of measures derived from the histogram including skewness, kurtosis, etc. (57). High resolution computed tomography (HRCT), enhances the resolving power of the image (58–62) allowing detection of less severe emphysema. Various computer-assisted texture based methods have successfully been used for tissue characterization. Traditional methods of texture analysis can be grouped into statistical, structural, and hybrid methods (63). Methods for tissue classification typically rely on region gray scale statistical measures (i.e.: mean, variance, frequency histogram) or textural measures (autocorrelation, co-occurrence matrices, run-length matrices, etc.) (46,47,55,57,64–74). Lung tissue can be objectively evaluated using the attenuation of lung tissue, either as mean lung attenuation, or by measuring the attenuation of lung falling below a set value (the density mask) (46,47,55, 57,73). It has been demonstrated that lung tissue mean attenuation can be an index of emphysema (46,47,55). However, a later study showed significant lung attenuation variation in normal individuals that could be misleading (73). To use attenuation distribution as a quantitative measure, much greater care needs to be taken to assure accurate scanner calibration in the air-water Hounsfield range and lung volumes at which scanning occurs need to be standardized. (75–79) Furthermore, one must consider that in a longitudinal pharmaceutical study lung attenuation is affected oppositely by changes in emphysema status and inflammation burden. A useful index of peripheral inflammation and airway disease has been a measure of air trapping. Quantitative tools to access air trapping have been shown to be quite sensitive. (80,81) A density masking approach alone is not sufficient to distinguish normal from diseased lung and Uppaluri et al. have introduced what has been dubbed the Adaptive Multiple Feature Method (AMFM).(82–84) This technique has utilized up to 26 different mathematical formulations to describe the gray scale heterogeneity of parenchymal regions within CT slices and then employed a Bayesian classifier to identify the best, small number of mathematical formulations (“features”) which distinguish one texture (pathologic state) from another.. More recently, Xu et al. (85,86) have shown that using volumetric images with isotropic voxels for 3D texture assessment provides significant improvements in the assessment of regional parenchymal pathology. In one test, Xu et al used the AMFM method, with appropriate training sets to accurately differentiate the CT scans of normal smokers from those of normal non-smokers. The use of the texture analysis method is only as good as the training sets developed, and if it is desirable to use the method for detection of parenchymal pathology undetectable by the human observer, training paradigms such as the one used by Xu must be established. Even when the training sets come from CT findings identified by human observers, the computer-based AMFM can be shown to be more consistent than human observers in its assessment of lung regions. Quantitation of lung images has become critical as pharmaceutical and device manufacturers seek to reduce the development time and seek to use imaging as a tool for the detection of regional lung changes (either a desired effect or an unwanted side effect) not reflected in the traditional pulmonary function tests which provide a global measure of the pulmonary physiology, but are relatively insensitive to regional changes. Figure 2 demonstrates a whole lung classification in which the AMFM simultaneously identified areas of emphysema (red), honeycomb pink), normal (blue), and ground glass (yellow). These data are from the work of Xu et al (204).

Functional imaging—Numerous imaging-based methods have been developed to assess ventilation, perfusion, or their functional outcome - gas exchange. Below we will show

examples of the use of MDCT imaging technology to probe normal and abnormal cardiopulmonary structure and function. We argue that MDCT technology offers a unique and comprehensive approach to evaluating the structural and functional complexity of the respiratory and cardiopulmonary systems.

Ventilation assessed by CT: The measurement of lung ventilation, lung volume, and tidal volume has traditionally been made for the entire lung, despite the fact that lung function in both health and disease is inhomogeneous. Attempts have been made to quantify regional ventilation both directly and indirectly with a variety of invasive techniques or radioisotope imaging (87–96), but these methods have been limited by invasiveness, poor spatial and temporal resolution, qualitative nature, and/or complexity. Xenon-enhanced MDCT (Xe-MDCT) is a method for the non-invasive measurement of regional pulmonary ventilation, determined from the wash-in and/or wash-out rates of the radiodense, non-radioactive gas xenon as measured in serially acquired, axial MDCT scans. Little work had been done since the original description of this technique nearly twenty five years ago (97–100), although the FDA approval of Xe-MDCT for measurement of cerebral blood flow has met with moderate clinical acceptance (101). Recently, however, the application of Xe-MDCT for measurement of regional pulmonary ventilation has been updated, validated, and refined including extension of the technique to estimate regional perfusion and V/Q (28,102–111) In Figure 3, we demonstrate a typical Xenon wash-in wash-out attenuation curve in a sheep, along with a color coded image of regional ventilation. Scanning was accomplished through gated imaging (end-expiration) as a fixed concentration of Xenon gas was inspired during the wash-in phase and then room air was inspired during wash-out. A mono-exponential curve is fitted to the wash-in or wash-out phase, providing a time constant as a measure of ventilation. Because the dynamic Xe-MDCT method requires the gated acquisition of axial CT images, timed so that the images are gathered at the same point in a series of standardized tidal breaths, the method has been most effectively applied to research animals breathing via respirators. The transfer of this methodology to humans has required the development of sophisticated feedback devices which monitor respiration via flow meters and displays which provide the subject with information related to targeted rate and depth of breathing information. Because of the complexity of such a system, there is considerable interest in the application of a single breath method utilizing dual energy CT. With the introduction of dual source CT, it is possible to image a subject during a breath hold following the inhalation of a single breath of a mixture of xenon and oxygen. With the kV of the two x-ray sources set to 80 and 140kV, it is possible to use material decomposition methods (19) to separate the xenon signal from the inherent x-ray attenuation of the lung. (21,22) Saba et al (21) have demonstrated the feasibility of such an approach, using 80 and 140 kV, during a single breath hold in a sheep. The images are presented in figure 4 showing the color coded xenon distribution superimposed upon the CT sections. In this sheep, a region of ventilation deficit in an area presenting with very subtle ground glass is demonstrated.

With the ability to retrospectively reconstruct 4D image data sets to represent a complete breathing cycle it becomes possible to assess regional ventilation through the use of image matching algorithms (12–18,112). Such image matching provides not only regional volume changes but also regional images of tissue strain, providing potential insights into local tissue properties such as early fibrosis, etc. The utility of such measures is only just now being investigated.

Perfusion assessed by CT—Dynamic imaging methods have been used to estimate arterial, venous, and capillary transit times and capillary flow distributions (113–120). These methods involve two types of image data collection regimes. Inlet-outlet detection is typically used for evaluating conducting vessels and whole organ analysis. The other data collection regime, referred to as residue detection, is typically used, alone or in conjunction with inlet

detection, for analysis of microvascular regions wherein the individual vessels are below the resolution of the imaging system. Various approaches for determining blood flow and/or mean transit time have been described (114,117–127). There have been a growing number of studies, demonstrating the use of MDCT with infusion of iodinated contrast agent to assess the presence of pulmonary emboli via visualization of flow voids in peripheral lung segments, and the improved ability to detect pulmonary emboli, aortic dissection and coronary atherosclerosis have resulted in the "triple ruleout" method for use in patients with chest pain (128). One must take care not to confuse this method to assess "flowing blood volume" with an assessment of true perfusion parameters. To assess regional parenchymal perfusion via dynamic axial MDCT, (129,130)we place a catheter in the right ventricular outflow tract in animals and in the superior vena cava in humans. A sharp (0.5 cc per kg over 2 seconds) bolus of iodinated contrast agent is delivered during ECG gated axial scanning. Scanning commences 1–2 heart beats prior to contrast injection with lungs held at functional residual capacity (FRC). By sampling the reconstructed time-attenuation curves within the region of a pulmonary artery and the lung parenchyma as shown in figure 5, we are able to calculate regional mean transit times, blood flow normalized to air or tissue content (131), and we are able to deconvolve the the signals such that we can estimate the timing of flow within the microvascular bed (129). In figure 5 we show a color coded image of a non-smoker and a smoker with normal pulmonary function tests but early CT findings of emphysema. Here, color coding provides a regional depiction of mean transit time. Using this approach, Alford et al(132) have demonstrated that heterogeneity of mean transit times is significantly increased in lung regions of smokers who have normal pulmonary function tests but who have very early CT evidence of emphysema. Through a series of publications recently (133–135)) Hoffman and colleagues have used functional CT imaging to demonstrate that hypoxic pulmonary vasoconstriction is normally blocked when hypoxic conditions are accompanied by inflammation. These observations have lead to the hypothesis that the failure of inherent mechanisms to block the normal hypoxic pulmonary vasoconstrictor (HPV) response of the pulmonary vasculature in the presence of inflammatory processes may lead to a failure of the normal response mechanisms serving to limit the inflammatory response and thus lead to the emphysema process. Figure 6 provides a demonstration of both an intact hypoxic pulmonary vasoconstrictor response as well as an inflammation-based blocking of the hypoxic pulmonary vasoconstrictor response in the same sheep. This animal had an endobronchial valve placed which allowed air out but not into a regional segment of the lung. At the same time, the animal arrived in the lab with regional pneumonia. The images demonstrate that in the region of the valve, there is a shunting of blood flow away from the hypoxic lung region while in the dependent regions of pneumonia, blood flow shunted away from the valve region is preferentially distributed to the region of inflammation because it presumably represents the path of least resistance. We show these images to demonstrate the power of advanced MDCT imaging to provide a link between structure and function.

MAGNETIC RESONANCE IMAGING

MRI has several advantages over CT, including speed of imaging, lack of ionizing radiation, ability to identify tissue characteristics and potential to obtain information on different nuclei allowing for novel approaches to lung function and micro-structure assessment.

Technical requirements

Most modern MR systems will be capable of obtaining excellent quality proton images of the chest. This will lead to relatively black lungs and excellent delineation of the chest wall, mediastinum and diaphragm. Parallel imaging sequences assist in obtaining images faster, within a single breath-hold, thus allowing for rapid image acquisition without the issue of motion artifact (136–138) A host of sequences are available, ranging from those focused on the diaphragm and mediastinum to those aimed at obtaining signal from the actual lungs

themselves. Using intravenous Gadolinium-based contrast agents, it is possible to delineate the pulmonary vascular tree as well as the right heart. Within the chest, MR images are almost always obtained during a single breath-hold, although dynamic imaging during a respiratory cycle is feasible (for instance to demonstrate diaphragm excursions). Ultrafast imaging is also capable of obtaining dynamic contrast images, leading to interpretation of pulmonary perfusion.

Proton imaging

As with any MRI technique, proton imaging uses the large magnetic field and the free moving protons to derive signal from changes in proton orientation due to radiofrequency pulses. The lungs are different from the rest of the body, as there is a relative low number of protons and most of the lung parenchyma consists of air. Although this is a problem, it can be used to advantage as pathological processes tend to increase the number of protons (hemorrhage, edema, inflammation, or tumor) or alternatively lead to relative voids of proton density (as with calcification or fibrosis).

The application of differently weighted sequences will lead to increase or decrease in proton signal. For instance, water will lead to increased signal on T2 weighted and decreased signal on T1 weighted sequences, whereas fat will have increased signal on both sequences. Moreover, it is possible to produce fat saturation pulses, resulting in complete depression of signal from fat.

In order to achieve faster imaging times, several techniques may be used. The oldest of these uses half-Fourier techniques, which only reconstruct slightly more than half the data space and extrapolate the missing data. This led to the single breath-hold sequences, which tend to be slightly T2 weighted, and that are also employed in a variety of other body imaging applications, such as MRCP. The newer MRI systems all have the ability to perform parallel imaging techniques, which is somewhat similar to multidetector row CT in that multiple slices are excited and read out simultaneously, thus increasing temporal resolution by a factor of 2–8.(136–138)

Although MRI has never really played a major role in routine chest imaging, several pathological processes can be evaluated using proton imaging, including pleural effusions, pneumonia, lung tumors (particularly useful in Pancoast tumors and for determination of tumor invasion in mesothelioma) and the assessment of the mediastinum (Figure 7). (139–141).The technique is complementary to CT, although tissue plane definition and characterization is better using MRI.

Assessment of respiratory dynamics has become feasible with the advent of ultrafast proton imaging capabilities. This has resulted in novel approaches for assessment of diaphragm and chest wall motion assessment and breathing mechanics.(142,143).

Gadolinium-enhanced imaging

The use of Gadolinium contrast has enabled a rapid expansion of chest MR imaging, as it became feasible to assess enhancement of pathological processes as well as visualization of the pulmonary vascular tree (both as static component and dynamics of perfusion) and the other large arteries. (144). This allowed MRI to become competitive with more traditional CT techniques in several aspects of chest imaging, particularly imaging of the large vessels, including congenital anomalies such as patent ductus arteriosus (Figure 8) and the assessment of pulmonary hypertension (Figure 9). (145,146) Although CT has maintained a primary role in the diagnosis of pulmonary embolism, the application of MRI for subsets of patients like

pregnant women or those that will require follow-up imaging to assess response to therapy is now feasible with very high-resolution MR angiographic imaging. (147–149)

In addition to the above described imaging techniques, MRI offers the possibility to assess perfusion of the lung vascular bed by ultra-fast imaging during the injection of Gadolinium contrast.(150,151) This enables direct visualization of regional perfusion, with the possibility of some form of quantification (though this is notoriously difficult in MRI due to signal-noise properties). Several studies have now demonstrated the feasibility of this technique for assessment of normal and pathological processes. (152–155) This application is now very close to general introduction into clinical practice.

Hyperpolarized gas imaging

MR imaging is versatile and has the capability to image other nuclei, including 3-Helium and 129-Xenon, provided the frequency of the system is adapted accordingly (for instance, for imaging 3-Helium at a field strength of 1.5 Tesla, the radiofrequency amplifier and transmit/receive radiofrequency coils are tuned to 48 MHz, compared with 64 Mhz for proton imaging). (156) Researchers discovered the potential of these noble, stable gas isotopes as a side-effect to nuclear physics experiments, which required hyperpolarization of 3-He to produce neutron mirrors. Hyperpolarization is a process whereby the atoms are brought to a higher energy level by introduction of laser light at the appropriate bandwidth. When this is achieved within a low magnetic field, the normally random population of spins will change to have a relatively higher population of atoms with spins aligned along the magnetic field. When this gas is introduced in a MRI environment, the usual RF frequency and response will result in enhanced signal, and this application successfully obtained the first images in the early-mid 1990s. (157–159)

Among the noble gases, the application of hyperpolarized 3-He has so far been widely used in clinical research studies, as the gas has better signal-to-noise ratio and remains in the airways without further interaction with the human body (in contrast to 129-Xe, which is lipid soluble and has anesthetic properties at higher concentrations). (156) However, improvement in hyperpolarization systems has meant that 129-Xenon MR imaging is making rapid strides forward, giving new insight in lung function. (160–162).One of the main features of hyperpolarized gas imaging is that the signal introduced in the system is so high that imaging is less dependent on field strength than is the case for proton imaging, and this has advantages as lower field-strength magnets may result in fewer artifacts. (163–165) A main disadvantage to this technique is that the contrast is exogenous, and is non-renewable. In order to maximize the use of the contrast, one must design special pulse sequences, to minimize loss of polarization by RF pulses and the paramagnetic effects of oxygen (more about this below). Several such techniques have been developed for hyperpolarized 3-Helium MRI and these have found a broad range of applications that may be of interest for the future assessment of pathophysiology as well as normal lung function and structure.

All hyperpolarized gas imaging techniques rely on the delivery of a single breath of gas mixture into the airways, with the hyperpolarization either performed on site or by a central distribution network. (166) This is usually achieved through the inhalation of the content of a plastic (Tedlar) bag, followed by a breath-hold lasting up to 16 seconds. Several thousands of applications have now taken place world-wide, and no significant adverse events have been observed. (167,168)

Ventilation distribution is built on the notion that any area with signal is a reflection of the delivery of 3-He gas to this area. It is possible to obtain a 3D volumetric dataset of the lungs using this technique (169), and several authors have shown the utility of this technique in normal volunteers, patients with asthma, emphysema (including alpha-1-antitrypsin deficiency; Figure 10A), cystic fibrosis (Figure 10B) and lung cancer (Figure 10C). (170–

177) There is homogeneous ventilation distribution in normal volunteers, although small ventilation defects are frequently seen. (170,178–180) In smoking subjects with normal pulmonary function tests, ventilation defects are usually already detectable. (181) In patients with emphysema, ventilation defects tend to be worse than in normal smokers and correlate with pulmonary function tests. (170,180) In asthmatic subjects, ventilation defects can be provoked using methacholine, and these are reversible using bronchodilator and correlate with pulmonary function tests (171,182) but quantification can be slightly more problematic. One method, using a subtraction of the proton MR mask from the hyperpolarized 3-He images has shown a very good repeatability with robust measurements and effectively yields “ventilated lung” as a percentage of overall chest cavity volume in a group of normal and smoking subjects. (183)

A limited study has been performed in patients with lung cancer, suggesting that it may be feasible to use hyperpolarized 3-He MRI as a tool for the planning of radiation fields, offering the possibility of higher tumor dose and sparing of relatively healthy lung and thereby the reduction of radiation pneumonitis. (177) Finally, limited studies in lung transplant recipients showed that 3-He MRI was capable of detecting abnormal ventilation (184) and more sensitive than HRCT or spirometry for the detection of bronchiolitis obliterans and ventilation abnormalities. (185,186)

Diffusion imaging is feasible, making use of the very high diffusivity of 3-He. When using several RF pulses separated by a pre-determined time interval, the MR system is capable of obtaining information on the distance traveled by the atoms. In a free open environment, this is significantly further compared to a restricted environment that exists within the lung and airways. Thus, the lung structure actually reduces the effective diffusion distance due to Brownian motion of 3-He atoms, leading to what is known as apparent diffusion coefficient (ADC) measurements, which are a direct representation of small airways size and correlated closely with histology. (187) Discussion has taken place whether these measurements represent terminal bronchioles, and different techniques are under development to assess longer or shorter measurement times, thus allowing for assessment of collateral ventilation (longer time scales) or true alveolar measurements (shorter time scales). (188,189)

ADC works by application of gradient echo pulse sequences at two different intervals, resulting in changes of polarization loss between more or less confined atoms. The ratio of these polarization changes allow the spatial mapping of ADC, with higher values allocated to larger air spaces (such as trachea and large bronchi). (190) ADC is homogeneously distributed in normal subjects, and becomes progressively more heterogeneous with normal smokers to emphysema (191–194). ADC has been shown to increase under the influence of aging (195, 196), emphysema (194,197,198) and due to gravity dependent compression of the lung (199); Figure 11). A significant issue is the fact that ADC measurements can only take place in areas where 3-He signal is present. In disease states with airway obstruction, such as seen in mucus plugging, this will affect the overall results.

Dynamic ventilation imaging enables the visualization of the 3-He signal as it flows into the main airways down to the peripheral airspaces, and makes use of a combination of ultra-fast imaging sequences and image reconstruction techniques that effectively interpolate the changes that occur during the imaging process, resulting in frame rate in the order of 5–10 ms. (200,201) . Ventilation can be quantified by obtaining curves of signal change during the imaging time, and it appears that the resulting curves closely correlate with (overall) lung function tests, as demonstrated in Figure 12 in a young patient with cystic fibrosis. (202,203) In addition, by prolonging the duration of the imaging process or by starting the MR data acquisition later in the respiratory cycle, it is possible to assess for regional airtrapping, which may be relevant in various types of airway outflow obstruction.

Oxygen sensitive imaging uses the paramagnetic effect of oxygen as a calculable decrease in the signal of 3-He due to loss of polarization. Thus, in areas where oxygen is absorbed rapidly (e.g. ventilation-perfusion matching) the signal of 3-He will remain, whereas areas where oxygen remains in the airways (e.g. ventilation-perfusion mismatch) demonstrate a faster signal loss. (204–206); It is now feasible to obtain 3D maps of oxygen uptake ratios (or ventilation-perfusion maps) using a single breath-hold technique. (207) The method is still under development, but may be able to assist, among many other options, the assessment of pulmonary thromboembolic disease (in particular chronic disease patients in the pre-operative assessment of thromboendarterectomy), the planning of surgical or endobronchial interventions and the pre-operative assessment of patients with borderline respectability of lung cancer. Several groups have demonstrated the feasibility of combining perfusion and ventilation studies in animal model settings .(208,209)

REFERENCES

1. Ritman, EL.; Robb, RA.; Harris, LD. Imaging Physiological Functions: Experience with the DSR. Philadelphia: Praeger; 1985.
2. Hoffman EA, Larsen RL. Regional Pulmonary Blood Flow via X-ray CT and Biodegradable Radiopaque Microspheres. Circulation 1990;4:111–124.
3. Boyd, DP.; Lipton, MJ. Cardiac computed tomography; Proceedings of the IEEE; 1983. p. 298-307.
4. Saito T, Misaki M, Shirato K, Takishima T. Three-dimensional quantitative coronary angiography. IEEE Trans Biomed Eng 1990;37:768–777. [PubMed: 2210785]
5. Saito Y. Multislice X-ray CT scanner. Medical Review 1998 Nov;98:1–8.
6. Wang G, Lin TH, Cheng PC, Shinozaki DM. A general cone-beam reconstruction algorithm. IEEE Trans Medical Imaging 1993;12:486–496.
7. McCollough CH, Primak AN, Saba O, et al. Dose performance of a 64-channel dual-source CT scanner. Radiology 2007;243:775–784. [PubMed: 17446525]
8. Flohr TG, McCollough CH, Bruder H, et al. First performance evaluation of a dual-source CT (DSCT) system. Eur Radiol 2006;16:256–268. [PubMed: 16341833]
9. Funabashi N, Mizuno N, Yoshida K, et al. Superiority of synchrony of 256-slice cone beam computed tomography for acquiring pulsating objects. Comparison with conventional multislice computed tomography. Int J Cardiol 2007;118:400–405. [PubMed: 17052785]
10. Mizuno N, Funabashi N, Imada M, Tsunoo T, Endo M, Komuro I. Utility of 256-slice cone beam tomography for real four-dimensional volumetric analysis without electrocardiogram gated acquisition. Int J Cardiol 2007;120:262–267. [PubMed: 17084925]
11. Saba OI, Chon D, Beck K, et al. Static versus prospective gated non-breath hold volumetric MDCT imaging of the lungs. Acad Radiol 2005;12:1371–1384. [PubMed: 16253849]
12. Xu S, Taylor RH, Fichtinger G, Cleary K. Lung deformation estimation and four-dimensional CT lung reconstruction. Acad Radiol 2006;13:1082–1092. [PubMed: 16935720]
13. Sarrut D, Boldea V, Miguet S, Ginestet C. Simulation of four-dimensional CT images from deformable registration between inhale and exhale breath-hold CT scans. Med Phys 2006;33:605–617. [PubMed: 16878564]
14. Guerrero T, Sanders K, Castillo E, et al. Dynamic ventilation imaging from four-dimensional computed tomography. Phys Med Biol 2006;51:777–791. [PubMed: 16467578]
15. Guerrero T, Sanders K, Noyola-Martinez J, et al. Quantification of regional ventilation from treatment planning CT. Int J Radiat Oncol Biol Phys 2005;62:630–634. [PubMed: 15936537]
16. Starkschall G, Desai N, Balter P, et al. Quantitative assessment of four-dimensional computed tomography image acquisition quality. J Appl Clin Med Phys 2007;8:2362. [PubMed: 17712299]
17. Rietzel E, Chen GT. Deformable registration of 4D computed tomography data. Med Phys 2006;33:4423–4430. [PubMed: 17153421]
18. Christensen GE, Song JH, Lu W, El Naqa I, Low DA. Tracking lung tissue motion and expansion/compression with inverse consistent image registration and spirometry. Med Phys 2007;34:2155–2163. [PubMed: 17654918]

19. Johnson TR, Nikolaou K, Fink C, et al. Dual-source CT in chest pain diagnosis. Radiologe 2007;47:301–309. [PubMed: 17285271]
20. Johnson TR, Krauss B, Sedlmair M, et al. Material differentiation by dual energy CT: initial experience. Eur Radiol 2007;17:1510–1517. [PubMed: 17151859]
21. Saba, OI.; Fuld, MK.; Krauss, B.; Van Beek, EJ.; McLennan, G.; Hoffman, EA. Dual Energy MDCT for Volumetric Assessment of V/Q: Initial Experiences; American Thoracic Society Annual Meeting; San Francisco, CA. 2007. p. A938
22. Fuld, M.; Saba, O.; Krauss, B.; Van Beek, EJ.; McClennan, G.; Hoffman, EA. Dual Energy Xe-MDCT for Automated Assessment of the Central airway Tree: initial Experiences; American Thoracic Society Annual Meeting; San Francisco, CA. 2007. p. A250
23. Remy-Jardin M, Pistolesi M, Goodman LR, et al. Management of suspected acute pulmonary embolism in the era of CT angiography: a statement from the Fleischner Society. Radiology 2007;245:315–329. [PubMed: 17848685]
24. Stillman AE, Oudkerk M, Ackerman M, et al. Use of multidetector computed tomography for the assessment of acute chest pain: a consensus statement of the North American Society of Cardiac Imaging and the European Society of Cardiac Radiology. Eur Radiol 2007;17:2196–2207. [PubMed: 17549487]
25. Wildberger JE, Klotz E, Ditt H, Spuntrup E, Mahnken AH, Gunther RW. Multislice computed tomography perfusion imaging for visualization of acute pulmonary embolism: animal experience. Eur Radiol 2005;15:1378–1386. [PubMed: 15776240]
26. Bayat S, Porra L, Suhonen H, Nemoz C, Suortti P, Sovijarvi AR. Differences in the time course of proximal and distal airway response to inhaled histamine studied by synchrotron radiation CT. J Appl Physiol 2006;100:1964–1973. [PubMed: 16469938]
27. Porra L, Monfraix S, Berruyer G, et al. Effect of tidal volume on distribution of ventilation assessed by synchrotron radiation CT in rabbit. J Appl Physiol 2004;96:1899–1908. [PubMed: 14966018]
28. Bayat S, Le Duc G, Porra L, et al. Quantitative functional lung imaging with synchrotron radiation using inhaled xenon as contrast agent. Phys Med Biol 2001;46:3287–3299. [PubMed: 11768506]
29. Keller JM, Edwards FM, Rundle R. Automatic outlining of regions on CT scans. Journal of Computer Assisted Tomography 1981;5:240–245. [PubMed: 7217448]
30. Kuhnigk H, Wunder C, Roewer N. Anaesthetic considerations for a 2-month-old infant with suspected complex I respiratory chain deficiency. Paediatr Anaesth 2003;13:83–85. [PubMed: 12535047]
31. Brown RH, Herold CJ, Hirshman CA, Zerhouni EA, Mitzner W. In vivo measurements of airway reactivity using high-resolution computed tomography. American Review of Respiratory Disease 1991;144:208–212. [PubMed: 2064130]
32. Amirav I, Kramer SS, Grunstein MM, Hoffman EA. Assessment of methacholine-induced airway constriction by ultrafast high-resolution computed tomography. Journal of Applied Physiology 1993;75:2239–2250. [PubMed: 8307884]
33. Brown RH, Herold CJ, Hirshman CA, Zerhouni EA, Mitzner W. Individual airway constrictor response heterogeneity to histamine assessed by high-resolution computed tomography. Journal of Applied Physiology 1993;74:2615–2620. [PubMed: 8365960]
34. Brown RH, Mitzner W, Zerhouni E, Hirshman CA. Direct in vivo visualization of bronchodilation induced by inhalational anesthesia using high-resolution computed tomography. Anesthesiology 1993;78:295–300. [PubMed: 8439025]
35. Zerhouni EA, Herold CJ, Brown RH, et al. High-resolution computed tomography-physiologic correlation. Journal of Thorac. Imaging 1993;8:265–272.
36. Brown RH, Herold C, Zerhouni EA, Mitzner W. Spontaneous airways constrict during breath holding studied by high-resolution computed tomography. Chest 1994;106:920–924. [PubMed: 8082378]
37. Palagyi K, Tschirren J, Hoffman EA, Sonka M. Quantitative analysis of pulmonary airway tree structures. Comput Biol Med 2006;36:974–996. [PubMed: 16076463]
38. Tschirren J, Hoffman EA, McLennan G, Sonka M. Intrathoracic airway trees: segmentation and airway morphology analysis from low dose CT scans. IEEE Trans Med Imaging 2005;24:1529–1539. [PubMed: 16353370]
39. Tschirren J, McLennan G, Palagyi K, Hoffman E, Sonka M. Matching and anatomical labeling of human airway tree. IEEE Trans Med Imaging 2005;24:1540–1547. [PubMed: 16353371]

40. Saba, OI.; Hoffman, EA.; Reinhardt, JM. Computed tomographic-based estimation of airway size with correction for scanned plane tilt angle. In: Chen, C-T.; Clough, AV., editors. SPIE Medical Imaging. San Diego, CA: 2000. p. 58-66.
41. Wood SA, Zerhouni EA, Hoford JD, Hoffman EA, Mitzner W. Measurement of three-dimensional lung tree structures by using computed tomography. Journal of Applied Physiology 1995;79:1687–1697. [PubMed: 8594030]
42. Hoffman EA, Clough AV, Christensen GE, et al. The comprehensive imaging-based analysis of the lung: a forum for team science. Acad Radiol 2004;11:1370–1380. [PubMed: 15596375]
43. Hoffman EA, Reinhardt JM, Sonka M, et al. Characterization of the interstitial lung diseases via density-based and texture-based analysis of computed tomography images of lung structure and function. Acad Radiol 2003;10:1104–1118. [PubMed: 14587629]
44. Nakano Y, Wong JC, de Jong PA, et al. The prediction of small airway dimensions using computed tomography. Am J Respir Crit Care Med 2005;171:142–146. [PubMed: 15516531]
45. Wananuki Y, Suzuki S, Nishikawa M, Miyashita A, Okubo T. Correlation of quantitative CT with selective alveolobronchogram and pulmonary function tests in emphysema. Chest 1994;106:806–813. [PubMed: 8082363]
46. Kinsella M, Muller NL, Abboud RT, Morrison NJ, DyBuncio A. Quantitation of Emphysema by computed tomography using a "density mask" program and correlation with pulmonary function tests. Chest 1990;97:315–321. [PubMed: 2298057]
47. Muller NL, Staples CA, Miller RR, Abboud RT. "Density mask". An objective method to quantitate emphysema using computed tomography. Chest 1988;94:782–787. [PubMed: 3168574]
48. Gould GA, Redpath AT, Ryan M, et al. Parenchymal emphysema measured by CT lung density correlates with lung function in patients with bullous disease. European Respiratory J 1993;6:698–704.
49. Stern EJ, Webb WR, Gamsu G. Dynamic quantitative computed tomography: A predictor of pulmonary function in obstructive lung diseases. Investigative Radiology 1994;29:564–569. [PubMed: 8077097]
50. Newman KB, Lynch DA, Newman LS, Ellegood D, Newell JD. Quantitative computed tomography detects air trapping due to asthma. Chest 1994;106:105–109. [PubMed: 8020254]
51. Millar AB, Fromson B, Strickland BA, Denison DM. Computed tomography based estimates of regional gas and tissue volume of the lung in supine subjects with chronic airflow limitation or fibrosing alveolitis. Thorax 1986;41:932–939. [PubMed: 3590056]
52. Rienmuller R, Behr J, Kalender WA. Standardized quantitative high resolution CT in lung diseases. Journal of Compututer Assissted Tomography 1991;15:742–749.
53. Biernacki W, Gould GA, Whyte KF, Flenley DC. Pulmonary hemodynamics, gas exchange, and the severity of emphysema as assessed by quantitative CT scan in chronic bronchitis and emphysema. American Review of Respiratory Disease 1989;139:1509–1515. [PubMed: 2729756]
54. Gould, KL. Coronary Artery Stenosis. New York: Elsevier; 1991.
55. Gould GA, Macnee W, McLean A, et al. CT Measurements of Lung Density in Life can quantitate distal airspace enlargement-an essential defining feature of human emphysema. American Review of Respiratory Disease 1988;137:380–392. [PubMed: 3341629]
56. Knudson RJ, Standen JR, Kaltenborn WT, et al. Expiratory computed tomography for assessmet of suspected pulmonary emphysema. Chest 1991;99:1357–1366. [PubMed: 2036816]
57. Hartley PG, Galvin JR, Hunninghake GW, et al. High-resolution CT-derived measures of lung density are valid indexes of interstitial lung disease. Journal of Applied Physiology 1994;76:271–277. [PubMed: 8175517]
58. Hruban RH, Meziane MA, Zerhouni EA, et al. High resolution computed tomography of inflation fixed lungs: pathologic-radiologic correlation of centrilobular emphysema. American Review of Respiratory Disease 1987;136:935–940. [PubMed: 3310774]
59. Miller RA, Muller NL, Vedal S, Morrison NJ, Staples CA. Limitations of computed tomography in the assessment of emphysema. American Review of Respiratory Disease 1989;139:980–983. [PubMed: 2930075]

60. Murata K, Itoh H, Senda M, et al. Stratified impairment of pulmonary ventilation in diffusepanbronchiolitis. PET and CT studies. Journal of Computer Assisted Tomography 1989;13:48–53. [PubMed: 2783429]
61. Webb WR. High-resolution computed tomography of the lung: Normal and abnormal anatomy. Seminars in Roentgenology 1991;26:110–117. [PubMed: 1853208]
62. Sanders C. Imaging of emphysema. Seminars in Respiratory Medicine 1992;13:318–330.
63. Sonka, M.; Hlavac, V.; Boyle, R. Image Processing, Analysis, and Machine Vision. London, New York: Chapman and Hall; 1993.
64. Schad LR, Bluml S, Zuna I. MR tissue characterization of intracranial tumors by means of texture analysis. Magnetic Resonance Imaging 1993;11:889–896. [PubMed: 8371644]
65. Miller P, Astley S. Classification of breast tissue by texture analysis. Image and Vision Computing 1992;10:277–282.
66. Wu C, Chen Y. Multi-threshold dimension vector for texture analysis and its application to liver tissue classification. Pattern Recognition 1993;1:137–144.
67. McPherson D, Aylward P, Knosp B, et al. Ultrasound chracterization of acute myocardial ischemia by quantitative texture analysis. Ultrasonic Imaging 1986;8:227–240. [PubMed: 3590424]
68. Skorton DJ, Collins SM, Nichols J, Pandian NG, Bean JA, Kerber RE. Quantitative texture analysis in two-dimensional echocardiography: Application to the diagnosis of experimental myocardial contusion. Circulation 1983;68:217–223. [PubMed: 6851048]
69. Chandrasekaran K, Aylward PE, Fleagle SR, et al. Feasibility of identifying amyloid and hypertrophic cardiomyopathy with the use of computerized quantitative texture analysis of clinical echocardiographic data. Journal of American College of Cardiology 1989;13:832–840.
70. Uppaluri, R.; Mitsa, T.; Galvin, JR. Fractal analysis of high-resolution CT images as a tool for quantification of lung diseases. In: Hoffman, EA., editor. Proc. SPIE Medical Imaging: Physiology and Function from Multidimensional Images; 1995. p. 133-142.
71. Tully RJ, Conners RW, Harlow CA, Lodwick GS. Towards computer analysis of pulmonary infiltration. Investigative Radiology 1978;13:298–305. [PubMed: 357340]
72. Katsuragawa S, Kunio D, MacMahon H. Image feature analysis and computer-aided diagnosis in digital radiography: Classification of normal and abnormal lungs with interstitial disease in chest images. Medical Physics 1989;16:38–44. [PubMed: 2646516]
73. Adams H, Bernard M, McConnochie K. An appraisal of CT pulmonary density mapping in normal subjects. Clinical Radiology 1991;43:238–242. [PubMed: 2025994]
74. Fleagle S, Stanford W, Burns T, Skorton D. Feasibility of quantitative texture analysis of cardiac magnetic resonance imagery: Preliminary results. SPIE Medical Imaging 1994;2168:23–32.
75. Yuan R, Mayo JR, Hogg JC, et al. The effects of radiation dose and CT manufacturer on measurements of lung densitometry. Chest 2007;132:617–623. [PubMed: 17573501]
76. Stolk J, Dirksen A, van der Lugt AA, et al. Repeatability of lung density measurements with low-dose computed tomography in subjects with alpha-1-antitrypsin deficiency-associated emphysema. Invest Radiol 2001;36:648–651. [PubMed: 11606842]
77. Shaker SB, Dirksen A, Laursen LC, Skovgaard LT, Holstein-Rathlou NH. Volume adjustment of lung density by computed tomography scans in patients with emphysema. Acta Radiol 2004;45:417–423. [PubMed: 15323394]
78. Parr DG, Stoel BC, Stolk J, Stockley RA. Validation of computed tomographic lung densitometry for monitoring emphysema in alpha1-antitrypsin deficiency. Thorax 2006;61:485–490. [PubMed: 16537666]
79. Bakker ME, Stolk J, Putter H, et al. Variability in densitometric assessment of pulmonary emphysema with computed tomography. Invest Radiol 2005;40:777–783. [PubMed: 16304481]
80. Matsuoka S, Kurihara Y, Yagihashi K, Nakajima Y. Quantitative assessment of peripheral airway obstruction on paired expiratory/inspiratory thin-section computed tomography in chronic obstructive pulmonary disease with emphysema. J Comput Assist Tomogr 2007;31:384–389. [PubMed: 17538284]
81. Goris ML, Zhu HJ, Blankenberg F, Chan F, Robinson TE. An automated approach to quantitative air trapping measurements in mild cystic fibrosis. Chest 2003;123:1655–1663. [PubMed: 12740287]

82. Uppaluri R, Hoffman E, Schwartz D, et al. Quantitative analysis of the chest CT in asbestos-exposed subjects using an adaptive multiple feature method. American Journal of Respiratory and Critical Care Medicine 1998;157:A276.

83. Uppaluri R, Mitsa T, Sonka M, Hoffman EA, McLennan G. Quantification of Pulmonary Emphysema from Lung CT Images Using Texture Analysis. Amer J Respir Crit Care Med 1997;156:248–254. [PubMed: 9230756]

84. Uppaluri R, McLennan G, Enright P, Hoffman E. AMFM - A quantitative assessment of early parenchymal changes in smokers. American Journal of Respiratory and Critical Care Medicine 1998;157:A788.

85. Xu Y, Sonka M, McLennan G, Guo J, Hoffman EA. MDCT-based 3-D texture classification of emphysema and early smoking related lung pathologies. IEEE Trans Med Imaging 2006;25:464–475. [PubMed: 16608061]

86. Xu Y, van Beek EJ, Hwanjo Y, Guo J, McLennan G, Hoffman EA. Computer-aided classification of interstitial lung diseases via MDCT: 3D adaptive multiple feature method (3D AMFM). Acad Radiol 2006;13:969–978. [PubMed: 16843849]

87. Ball W, Stewart P, Newsham L, Bates D. Regional pulmonary function studied with Xenon133. Journal of Clinical Investigation 1962;41:519–531. [PubMed: 13864417]

88. Jones R, Overton T, Sproule B. Frequency dependence of ventilation distribution in normal and obstructed lungs. Journal of Applied Physiology 1977;42:548–553. [PubMed: 863816]

89. Bunow B, Line B, Horton M, Weiss G. Regional ventilatory clearance by xenon scintigraphy: a critical evaluation of two estimation procedures. J Nucl Med 1979;20:703–710. [PubMed: 541708]

90. Hubmayr R, Walters B, Chevalier PA, Rodarte JR, Olson LE. Topographical distribution of regional lung volume in anesthetized dogs. Journal of Applied Physiology 1983;54:1048–1056. [PubMed: 6853280]

91. Fredberg J, Keefe D, Glass G, Castile R, Frantz Id. Alveolar pressure nonhomogeneity during small-amplitude high-frequency oscillation. Journal of Applied Physiology 1984;57:788–800. [PubMed: 6490465]

92. van der Mark T, Rookmaker A, Kiers A, et al. Nitrogen-13 and xenon-133 ventilation studies. Journal of Nuclear Medicine 1984;25:1175–1182. [PubMed: 6491748]

93. Berdine G, Lehr J, McKinley D, Drazen J. Nonuniformity of canine lung washout by high-frequency ventilation. Journal of Applied Physiology 1986;61:1388–1394. [PubMed: 3781955]

94. Venegas J, Yamada Y, Custer J, Hales C. Effects of respiratory variables on regional gas transport during high-frequency ventilation. Journal of Applied Physiology 1988;64:2108–2118. [PubMed: 3391909]

95. Hubmayr R, Hill M, Wilson T. Nonuniform expansion of constricted dog lungs. Journal of Applied Physiology 1996;80:522–530. [PubMed: 8929594]

96. Robertson H, Glenny R, Stanford D, McInnes L, Luchtel D, Covert D. High-resolution maps of regional ventilation utilizing inhaled fluorescent microspheres. Journal of Applied Physiology 1997;82:943–953. [PubMed: 9074986]

97. Gur D, Drayer BP, Borovetz HS, Griffith BP, Hardesty RL, Wolfson SK. Dynamic computed tomography of the lung: Regional ventilation measurements. J. Comp. Asst. Tomog 1979;3:749–753.

98. Gur D, Shabason L, Borovetz HS, et al. Regional pulmonary ventilation measurements by Xenon enhanced dynamic computed tomography: An update. J. Comp. Asst. Tomog 1981;5:678–683.

99. Snyder J, Pennock B, Herbert D, et al. Local lung ventilation in critically ill patients using nonradioactive xenon-enhanced transmission computed tomography. Crit Care Med 1984;12:46–51. [PubMed: 6360534]

100. Murphy DMF, Nicewicz JT, Zabbatino SM, Moore RA. Local pulmonary ventilation using nonradioactive xenon-enhanced ultrafast computed tomography. Chest 1989;96:799–804. [PubMed: 2791675]

101. Yonas H, Jungreis C. Xenon CT cerebral blood flow: past, present, and future. AJNR American Journal of Neuroradiology 1995;16:219–220. [PubMed: 7900599]

102. Marcucci C, Simon B. Distribution of regional pulmonary ventilation in prone and supine dogs using xenon-enhanced CT. Faseb Journal 1996;10:A363.

103. Simon B, Marcucci C, et al. CT measurement of regional specific compliance correlates with specific ventilation in intact dogs. Am. J. Resp. Crit. Care Med. 1999in press
104. Simon B, Chandler D. Regional differences in volume recruitment and ventilation in dogs after acute lung injury (ALI). Am. J. Resp. Crit. Care Med 1998;157:A214.
105. Tajik JK, Tran BQ, Hoffman EA. Xenon enhanced CT imaging of local pulmonary ventilation. SPIE Medical Imaging Physiology and Function from Multidimensional Images 1996;2709:40–54.
106. Simon B, Marcucci C, et al. Parameter estimation and confidence intervals for Xe-CT ventilation studies: a Monte Carlo approach. J Appl Physiol 1998;84:709–716. [PubMed: 9475884]
107. Tajik JK, Chon D, Won C, Tran BQ, Hoffman EA. Subsecond multisection CT of regional pulmonary ventilation. Acad Radiol 2002;9:130–146. [PubMed: 11918366]
108. Suga K. Technical and analytical advances in pulmonary ventilation SPECT with xenon-133 gas and Tc-99m-Technegas. Ann Nucl Med 2002;16:303–310. [PubMed: 12230089]
109. Kreck TC, Krueger MA, Altemeier WA, et al. Determination of regional ventilation and perfusion in the lung using xenon and computed tomography. J Appl Physiol 2001;91:1741–1749. [PubMed: 11568158]
110. Chon D, Simon BA, Beck KC, et al. Differences in regional wash-in and wash-out time constants for xenon-CT ventilation studies. Respir Physiol Neurobiol 2005;148:65–83. [PubMed: 16061426]
111. Chon D, Beck KC, Simon BA, Shikata H, Saba OI, Hoffman EA. Effect of low-xenon and krypton supplementation on signal/noise of regional CT-based ventilation measurements. J Appl Physiol 2007;102:1535–1544. [PubMed: 17122371]
112. Coselmon MM, Balter JM, McShan DL, Kessler ML. Mutual information based CT registration of the lung at exhale and inhale breathing states using thin-plate splines. Med Phys 2004;31:2942–2948. [PubMed: 15587645]
113. Ayappa I, Brown LV, Wang PM, Lai-Fook SJ. Arterial, capillary, and venous transit times and dispersion measured in isolated rabbit lungs. Journal of Applied Physiology 1995;79:261–269. [PubMed: 7559230]
114. Capen RL, Latham LP, Wagner WW Jr. Comparison of direct and indirect measurements of pulmonary capillary transit times. Journal of Applied Physiology 1987;62:1150–1154. [PubMed: 3571071]
115. Clough AV, Linehan JH, Dawson C. Regional perfusion parameters from pulmonary microfocal angiograms. American Journal of Physiology 1997;272:H1537–H1548. [PubMed: 9087632]
116. Clough AV, Haworth ST, Hanger CC, et al. Transit time dispersion in the pulmonary arterial tree. Journal of Applied Physiology 1998;85:565–574. [PubMed: 9688734]
117. Hoffman EA, Tajik JK. Dynamic and high resolution CT assessment of pulmonary blood flow distributions. Am Rev Resp Dis 1993;147:A201.
118. Mintun MA, Ter-Pergossian MM, Green MA, Lich LL, Schuster DP. Quantitative measurement of regional pulmonary blood flow with positron emission tomography. Journal of Applied Physiology 1986;60:317–326. [PubMed: 3484739]
119. Tajik, JK.; Tan, BQ.; Hoffman, EA. CT-based assessment of regional pulmonary blood flow parameters. In: Chen, C-T.; Clough, AV., editors. Medical Imaging 1999: Physiology and function from multidimensional images. San Diego: SPIE; 1999. p. 181-187.
120. Wolfkiel CJ, Rich S. Analysis of regional pulmonary enhancement in dogs by ultrafast computed tomography. Invest. Radiology 1992;27:211–216.
121. Bassingthwaighte, JB.; Raymond, GR.; Chan, JIS. Principles of tracer kinetics. In: Zaret, BL.; Beller, GA., editors. Nuclear cardiology: State of the art and future directions. St. Louis, MO: 1993. p. 3-23.
122. Bentley MD, Lerman LO, Hoffman EA, Fiksen-Olsen MJ, Ritman EL, Romero JC. Measurement of renal perfusion and blood flow with fast computed tomography. Circ Res 1994;74:945–951. [PubMed: 8156641]
123. Eigler NL, Schuhlen H, Whiting JS, Pfaff JM, Zeiher A, Gu S. Digital angiographic impulse response analysis of regional myocardial perfusion. Estimation of coronary flow, flow reserve, and distribution volume by compartmental transit time measurement in a canine model. Circ Res 1991;68:870–880. [PubMed: 1742872]

124. Ritman EL. Temporospatial heterogeneity of myocardial perfusion and blood volume in the porcine heart wall. Ann Biomed Eng 1998;26:519–525. [PubMed: 9662144]
125. Musch G, Layfield JD, Harris RS, et al. Topographical distribution of pulmonary perfusion and ventilation, assessed by PET in supine and prone humans. J Appl Physiol 2002;93:1841–1851. [PubMed: 12381773]
126. Levin DL, Chen Q, Zhang M, Edelman RR, Hatabu H. Evaluation of regional pulmonary perfusion using ultrafast magnetic resonance imaging. Magn Reson Med 2001;46:166–171. [PubMed: 11443723]
127. Hatabu H, Tadamura E, Levin DL, et al. Quantitative assessment of pulmonary perfusion with dynamic contrast-enhanced MRI. Magn Reson Med 1999;42:1033–1038. [PubMed: 10571924]
128. Johnson TR, Nikolaou K, Wintersperger BJ, et al. ECG-gated 64-MDCT angiography in the differential diagnosis of acute chest pain. AJR Am J Roentgenol 2007;188:76–82. [PubMed: 17179348]
129. Won C, Chon D, Tajik J, et al. CT-based assessment of regional pulmonary microvascular blood flow parameters. J Appl Physiol 2003;94:2483–2493. [PubMed: 12588787]
130. Chon D, Beck KC, Larsen RL, Shikata H, Hoffman EA. Regional pulmonary blood flow in dogs by 4D-X-ray CT. J Appl Physiol 2006;101:1451–1465. [PubMed: 16825517]
131. Hoffman EA, Tajik JK, Kugelmass SD. Matching pulmonary structure and perfusion via combined dynamic multislice CT and thin-slice high-resolution CT. Comput Med Imaging Graph 1995;19:101–112. [PubMed: 7736410]
132. Alford, SK.; Van Beek, EJ.; McLennan, G.; Hoffman, EA. Characterization of Smoking Related Regional Alterations in Pulmonary Perfusion Via Functional CT; American Thoracic Society Annual Meeting; San Francisco, CA. 2007. p. A818
133. Fuld, M.; Chon, D.; Milchak, R.; McLennan, G.; Simon, BA.; Hoffman, EA. Global pulmonary hypoxia causes enhanced perfusion in regions of local inflammation; American Thoracic Society Annual Meeting; San Diego, CA. 2006. p. A330
134. Easley RB, Fuld MK, Fernandez-Bustamante A, Hoffman EA, Simon BA. Mechanism of hypoxemia in acute lung injury evaluated by multidetector-row CT. Acad Radiol 2006;13:916–921. [PubMed: 16777566]
135. Hoffman, EA.; Simon, BA.; McLennan, G. State of the Art. A structural and functional assessment of the lung via multidetector-row computed tomography: phenotyping chronic obstructive pulmonary disease; Proc Am Thorac Soc; 2006. p. 519-532.
136. Yeh EN, Stuber M, McKenzie CA, et al. Inherently self-calibrating non-Cartesian parallel imaging. Magn Reson Med 2005;54:1–8. [PubMed: 15968671]
137. Sodickson DK, Manning WJ. Simultaneous acquisition of spatial harmonics (SMASH): fast imaging with radiofrequency coil arrays. Magn Reson Med 1997;38:591–603. [PubMed: 9324327]
138. Pruessmann KP, Weiger M, Scheidegger MB, Boesiger P. SENSE: sensitivity encoding for fast MRI. Magn Reson Med 1999;42:952–962. [PubMed: 10542355]
139. Benamore RE, O'Doherty MJ, Entwisle JJ. Use of imaging in the management of malignant pleural mesothelioma. Clin Radiol 2005;60:1237–1247. [PubMed: 16291305]
140. Erasmus JJ, Truong MT, Munden RF. CT, MR, and PET imaging in staging of nonsmall-cell lung cancer. Semin Roentgenol 2005;40:126–142. [PubMed: 15898410]
141. Puderbach M, Hintze C, Ley S, Eichinger M, Kauczor HU, Biederer J. MR imaging of the chest: A practical approach at 1.5T. Eur J Radiol. 2007
142. Swift AJ, Woodhouse N, Fichele S, et al. Rapid lung volumetry using ultrafast dynamic magnetic resonance imaging during forced vital capacity maneuver: correlation with spirometry. Invest Radiol 2007;42:37–41. [PubMed: 17213747]
143. Eichinger M, Tetzlaff R, Puderbach M, Woodhouse N, Kauczor HU. Proton magnetic resonance imaging for assessment of lung function and respiratory dynamics. Eur J Radiol. 2007
144. Pedersen MR, Fisher MT, van Beek EJ. MR imaging of the pulmonary vasculature--an update. Eur Radiol 2006;16:1374–1386. [PubMed: 16391908]
145. Kreitner KF, Kunz RP, Ley S, et al. Chronic thromboembolic pulmonary hypertension - assessment by magnetic resonance imaging. Eur Radiol 2007;17:11–21. [PubMed: 16838142]

146. Ley S, Zaporozhan J, Arnold R, et al. Preoperative assessment and follow-up of congenital abnormalities of the pulmonary arteries using CT and MRI. Eur Radiol 2007;17:151–162. [PubMed: 16799783]

147. Meaney JF, Weg JG, Chenevert TL, Stafford-Johnson D, Hamilton BH, Prince MR. Diagnosis of pulmonary embolism with magnetic resonance angiography. N Engl J Med 1997;336:1422–1427. [PubMed: 9145679]

148. Oudkerk M, van Beek EJ, Wielopolski P, et al. Comparison of contrast-enhanced magnetic resonance angiography and conventional pulmonary angiography for the diagnosis of pulmonary embolism: a prospective study. Lancet 2002;359:1643–1647. [PubMed: 12020524]

149. Ohno Y, Higashino T, Takenaka D, et al. MR angiography with sensitivity encoding (SENSE) for suspected pulmonary embolism: comparison with MDCT and ventilation-perfusion scintigraphy. AJR Am J Roentgenol 2004;183:91–98. [PubMed: 15208117]

150. Iwasawa T, Saito K, Ogawa N, Ishiwa N, Kurihara H. Prediction of postoperative pulmonary function using perfusion magnetic resonance imaging of the lung. J Magn Reson Imaging 2002;15:685–692. [PubMed: 12112519]

151. Fink C, Puderbach M, Ley S, Zaporozhan J, Plathow C, Kauczor HU. Time-resolved echo-shared parallel MRA of the lung: observer preference study of image quality in comparison with non-echo-shared sequences. Eur Radiol 2005;15:2070–2074. [PubMed: 15988585]

152. Ohno Y, Hatabu H, Murase K, et al. Primary pulmonary hypertension: 3D dynamic perfusion MRI for quantitative analysis of regional pulmonary perfusion. AJR Am J Roentgenol 2007;188:48–56. [PubMed: 17179345]

153. Ley S, Mereles D, Risse F, et al. Quantitative 3D pulmonary MR-perfusion in patients with pulmonary arterial hypertension: correlation with invasive pressure measurements. Eur J Radiol 2007;61:251–255. [PubMed: 17045440]

154. Hopkins SR, Garg J, Bolar DS, Balouch J, Levin DL. Pulmonary blood flow heterogeneity during hypoxia and high-altitude pulmonary edema. Am J Respir Crit Care Med 2005;171:83–87. [PubMed: 15486339]

155. Roeleveld RJ, Marcus JT, Boonstra A, et al. A comparison of noninvasive MRI-based methods of estimating pulmonary artery pressure in pulmonary hypertension. J Magn Reson Imaging 2005;22:67–72. [PubMed: 15971176]

156. Goodson BM. Nuclear magnetic resonance of laser-polarized noble gases in molecules, materials, and organisms. J Magn Reson 2002;155:157–216. [PubMed: 12036331]

157. Albert MS, Cates GD, Driehuys B, et al. Biological magnetic resonance imaging using laser-polarized 129Xe. Nature 1994;370:199–201. [PubMed: 8028666]

158. Middleton H, Black RD, Saam B, et al. MR imaging with hyperpolarized 3He gas. Magn Reson Med 1995;33:271–275. [PubMed: 7707920]

159. Black RD, Middleton HL, Cates GD, et al. In vivo He-3 MR images of guinea pig lungs. Radiology 1996;199:867–870. [PubMed: 8638019]

160. Ruset, I.; Hersman, F. Novel low-pressure production method for hyperpolarized Xenon; Proceddings of the 11th Annual Scientific Meeting of the ISMRM; 2003.

161. Ruset IC, Ketel S, Hersman FW. Optical pumping system design for large production of hyperpolarized. Phys Rev Lett 2006;96053002

162. Patz S, Hersman FW, Muradian I, et al. Hyperpolarized (129)Xe MRI: A viable functional lung imaging modality? Eur J Radiol. 2007

163. Darasse L, Guillot G, Nacher P, Tastevin G. Low-field 3He nuclear magnetic resonance in human lungs. CR Acad Sci II B 1997;324:691–700.

164. Durand E, Guillot G, Darrasse L, et al. CPMG measurements and ultrafast imaging in human lungs with hyperpolarized helium-3 at low field (0.1 T). Magn Reson Med 2002;47:75–81. [PubMed: 11754445]

165. Mair RW, Hrovat MI, Patz S, et al. 3He lung imaging in an open access, very-low-field human magnetic resonance imaging system. Magn Reson Med 2005;53:745–749. [PubMed: 15799045]

166. Wild JM, Schmiedeskamp J, Paley MN, et al. MR imaging of the lungs with hyperpolarized helium-3 gas transported by air. Phys Med Biol 2002;47:N185–N190. [PubMed: 12164592]

167. de Lange, E.; Altes, T.; Wright, C.; Mata, J.; Harding, D.; Harrell, F. Hyperbolized gas MR imaging of the lung: safety assessment of inhaled helium-3; Proceedings of the 89th Scientific Assembly and Annual Meeting of the Radiological Society of North America; Chicago. 2003.
168. Woodhouse, N.; Wild, J.; Mills, G.; Fleming, S.; Fichele, S.; van Beek, EJ. Comparision of hyperolarized 3 He adminstration methods in healthly and diseased subjects; Proceedings 14th Annual Scientific Meeting ISMRM; Seattle. 2006.
169. Wild JM, Woodhouse N, Paley MN, et al. Comparison between 2D and 3D gradient-echo sequences for MRI of human lung ventilation with hyperpolarized 3He. Magn Reson Med 2004;52:673–678. [PubMed: 15334590]
170. van Beek E, Wild J, Schreiber W, Kauczor H, Mugler JP 3rd, de Lange EE. Functional MRI of the lungs using hyperpolarized 3-helium gas. J Magn Reson Imaging 2004;20:540–554. [PubMed: 15390146]
171. de Lange EE, Altes TA, Patrie JT, et al. Evaluation of asthma with hyperpolarized helium-3 MRI: correlation with clinical severity and spirometry. Chest 2006;130:1055–1062. [PubMed: 17035438]
172. de Lange EE, Altes TA, Patrie JT, et al. The variability of regional airflow obstruction within the lungs of patients with asthma: assessment with hyperpolarized helium-3 magnetic resonance imaging. J Allergy Clin Immunol 2007;119:1072–1078. [PubMed: 17353032]
173. Donnelly LF, MacFall JR, McAdams HP, et al. Cystic fibrosis: combined hyperpolarized 3He-enhanced and conventional proton MR imaging in the lung--preliminary observations. Radiology 1999;212:885–889. [PubMed: 10478261]
174. van Beek EJ, Hill C, Woodhouse N, et al. Assessment of lung disease in children with cystic fibrosis using hyperpolarized 3-Helium MRI: comparison with Shwachman score, Chrispin-Norman score and spirometry. Eur Radiol 2007;17:1018–1024. [PubMed: 16941089]
175. McMahon C, Dodd J, Hill C, et al. Hyperpolarized 3Helium magnetic resonance ventilation imaging in patients with cystic fibrosis: correlation with high resolution CT and spirometry. Eur Radiol 2006;16:2483–2490. [PubMed: 16871384]
176. Mentore K, Froh DK, de Lange EE, Brookeman JR, Paget-Brown AO, Altes TA. Hyperpolarized HHe 3 MRI of the lung in cystic fibrosis: assessment at baseline and after bronchodilator and airway clearance treatment. Acad Radiol 2005;12:1423–1429. [PubMed: 16253854]
177. Ireland RH, Bragg CM, McJury M, et al. Feasibility of image registration and intensity-modulated radiotherapy planning with hyperpolarized helium-3 magneticz resonance imaging for non-small-cell lung cancer. Int J Radiat Oncol Biol Phys 2007;68:273–281. [PubMed: 17448880]
178. MacFall JR, Charles HC, Black RD, et al. Human lung air spaces: potential for MR imaging with hyperpolarized He-3. Radiology 1996;200:553–558. [PubMed: 8685356]
179. Kauczor HU, Hofmann D, Kreitner KF, et al. Normal and abnormal pulmonary ventilation: visualization at hyperpolarized He-3 MR imaging. Radiology 1996;201:564–568. [PubMed: 8888259]
180. de Lange EE, Mugler JP 3rd, Brookeman JR, et al. Lung air spaces: MR imaging evaluation with hyperpolarized 3He gas. Radiology 1999;210:851–857. [PubMed: 10207491]
181. Guenther D, Eberle B, Hast J, et al. (3)He MRI in healthy volunteers: preliminary correlation with smoking history and lung volumes. NMR Biomed 2000;13:182–189. [PubMed: 10867694]
182. Samee S, Altes T, Powers P, et al. Imaging the lungs in asthmatic patients by using hyperpolarized helium-3 magnetic resonance: assessment of response to methacholine and exercise challenge. J Allergy Clin Immunol 2003;111:1205–1211. [PubMed: 12789218]
183. Woodhouse N, Wild JM, Paley MN, et al. Combined helium-3/proton magnetic resonance imaging measurement of ventilated lung volumes in smokers compared to never-smokers. J Magn Reson Imaging 2005;21:365–369. [PubMed: 15779032]
184. McAdams HP, Palmer SM, Donnelly LF, Charles HC, Tapson VF, MacFall JR. Hyperpolarized 3He-enhanced MR imaging of lung transplant recipients: preliminary results. AJR Am J Roentgenol 1999;173:955–959. [PubMed: 10511156]
185. Zaporozhan J, Ley S, Gast KK, et al. Functional analysis in single-lung transplant recipients: a comparative study of high-resolution CT, 3He-MRI, and pulmonary function tests. Chest 2004;125:173–181. [PubMed: 14718438]

186. Gast KK, Zaporozhan J, Ley S, et al. (3)He-MRI in follow-up of lung transplant recipients. Eur Radiol 2004;14:78–85. [PubMed: 14564471]

187. Woods JC, Choong CK, Yablonskiy DA, et al. Hyperpolarized 3He diffusion MRI and histology in pulmonary emphysema. Magn Reson Med 2006;56:1293–1300. [PubMed: 17058206]

188. Woods JC, Yablonskiy DA, Choong CK, et al. Long-range diffusion of hyperpolarized 3He in explanted normal and emphysematous human lungs via magnetization tagging. J Appl Physiol 2005;99:1992–1997. [PubMed: 16024528]

189. Wang C, Miller GW, Altes TA, de Lange EE, Cates GD Jr, Mugler JP 3rd. Time dependence of 3He diffusion in the human lung: measurement in the long-time regime using stimulated echoes. Magn Reson Med 2006;56:296–309. [PubMed: 16791861]

190. Morbach AE, Gast KK, Schmiedeskamp J, et al. Diffusion-weighted MRI of the lung with hyperpolarized helium-3: a study of reproducibility. J Magn Reson Imaging 2005;21:765–774. [PubMed: 15906344]

191. Saam BT, Yablonskiy DA, Kodibagkar VD, et al. MR imaging of diffusion of (3)He gas in healthy and diseased lungs. Magn Reson Med 2000;44:174–179. [PubMed: 10918314]

192. Owers-Bradley JR, Fichele S, Bennattayalah A, et al. MR tagging of human lungs using hyperpolarized 3He gas. J Magn Reson Imaging 2003;17:142–146. [PubMed: 12500284]

193. Schreiber WG, Morbach AE, Stavngaard T, et al. Assessment of lung microstructure with magnetic resonance imaging of hyperpolarized Helium-3. Respir Physiol Neurobiol 2005;148:23–42. [PubMed: 15967737]

194. Swift AJ, Wild JM, Fichele S, et al. Emphysematous changes and normal variation in smokers and COPD patients using diffusion 3He MRI. Eur J Radiol 2005;54:352–358. [PubMed: 15899335]

195. Fain SB, Altes TA, Panth SR, et al. Detection of age-dependent changes in healthy adult lungs with diffusion-weighted 3He MRI. Acad Radiol 2005;12:1385–1393. [PubMed: 16253850]

196. Altes TA, Mata J, de Lange EE, Brookeman JR, Mugler JP 3rd. Assessment of lung development using hyperpolarized helium-3 diffusion MR imaging. J Magn Reson Imaging 2006;24:1277–1283. [PubMed: 17096396]

197. Salerno M, de Lange EE, Altes TA, Truwit JD, Brookeman JR, Mugler JP 3rd. Emphysema: hyperpolarized helium 3 diffusion MR imaging of the lungs compared with spirometric indexes--initial experience. Radiology 2002;222:252–260. [PubMed: 11756734]

198. Fain SB, Panth SR, Evans MD, et al. Early emphysematous changes in asymptomatic smokers: detection with 3He MR imaging. Radiology 2006;239:875–883. [PubMed: 16714465]

199. Fichele S, Woodhouse N, Said Z, et al. MRI of Helium-3 Gas in Healthy Lungs: Posture Related Variations of Alveolar Size. J Magn Reson Imaging 2004;20:331–335. [PubMed: 15269962]

200. Salerno M, Altes TA, Brookeman JR, de Lange EE, Mugler JP 3rd. Dynamic spiral MRI of pulmonary gas flow using hyperpolarized (3)He: preliminary studies in healthy and diseased lungs. Magn Reson Med 2001;46:667–677. [PubMed: 11590642]

201. Wild JM, Paley MN, Kasuboski L, et al. Dynamic radial projection MRI of inhaled hyperpolarized 3He gas. Magn Reson Med 2003;49:991–997. [PubMed: 12768575]

202. Dupuich D, Berthezene Y, Clouet PL, Stupar V, Canet E, Cremillieux Y. Dynamic 3He imaging for quantification of regional lung ventilation parameters. Magn Reson Med 2003;50:777–783. [PubMed: 14523964]

203. Koumellis P, EJR vB, Hill C, et al. Quantitative analysis of regional airways obstruction using dynamic hyperpolarized 3He MRI - preliminary results in children with cystic fibrosis. JMRI 2005:420–426. [PubMed: 16104046]

204. Eberle B, Weiler N, Markstaller K, et al. Analysis of intrapulmonary O(2) concentration by MR imaging of inhaled hyperpolarized helium-3. J Appl Physiol 1999;87:2043–2052. [PubMed: 10601148]

205. Deninger AJ, Eberle B, Ebert M, et al. (3)he-MRI-based measurements of intrapulmonary p(O2) and its time course during apnea in healthy volunteers: first results, reproducibility, and technical limitations. NMR Biomed 2000;13:194–201. [PubMed: 10867696]

206. Deninger AJ, Eberle B, Bermuth J, et al. Assessment of a single-acquisition imaging sequence for oxygen-sensitive (3)He-MRI. Magn Reson Med 2002;47:105–114. [PubMed: 11754449]

207. Wild JM, Fichele S, Woodhouse N, Paley MN, Kasuboski L, van Beek EJ. 3D volume-localized pO2 measurement in the human lung with 3He MRI. Magn Reson Med 2005;53:1055–1064. [PubMed: 15844148]

208. Cremillieux Y, Berthezene Y, Humblot H, et al. A combined 1H perfusion/3He ventilation NMR study in rat lungs. Magn Reson Med 1999;41:645–648. [PubMed: 10332838]

209. Hong C, Leawoods JC, Yablonskiy DA, et al. Feasibility of combining MR perfusion, angiography, and 3He ventilation imaging for evaluation of lung function in a porcine model. Acad Radiol 2005;12:202–209. [PubMed: 15721597]

Glossary

Apparent diffusion coefficient, A measure of the peripheral air space size in the lung as assessed via polarized gas methods

Attenuation, The unit of measure of a CT scan related to regional lung tissue density

Density mask, A measure of the number of voxels in a region of interest (such as the lung field) which fall below or above a given Hounsfield Unit

Dual energy CT, Use of CT images obtained with the x-ray guns set at two different kilo voltage settings (such as 80 and 140kV) to allow for the seperation coincident materials such as tissue and iodine or iodine and bone, etc.

Dual source CT, Use of two x-ray guns and associated detector rows on a single rotating gantry to allow for more rapid acquisition of projection images used in the image reconstruction process. This reduces motion blur of rapidly moving structures such as the heart and allows for the use of dual energy imaging for the separation of coincident materials. (see above)

Dynamic scan, Imaging in an axial mode in rapid succession either through timing or gating to a physiological signal. The temporal series of images are used to assess physiological events such as respiration, blood flow, cardiac wall contraction, etc.

Gating, Timing of image acquisition (projection images in the case of CT scanning) such that the projection images are gathered at a fixed point of a physiological cycle such as a particular point in the respiratory or cardiac cycles.

Gray scale, A scaled representation of the x-ray attenuation coefficients within the reconstructed cross sections produced through the process of CT imaging.

Hounsfield units, A scaled representation of the x-ray attenuation coefficient also refered to as the image "gray scale." Air is −1000, water is 0 and dense bone is +1000.

Multi-detector row CT (MDCT), A CT scanner which utilizes a cone beam x-ray source, coupled with more than one row of juxtaposed detectors to allow for the more rapid acquistion of projection data used to reconstruct CT cross sectional images. Currently scanners are available for clinical use with up to 320 rows of detectors.

Pitch, Table travel divided by the total collimation of the x-ray beam.

Scan aperture, Time required to generate the projections used in the reconstruction of a CT slice. This may take the form of an effective scan aperture if a short period of time within multiple physiological cycles are used in the reconstruction process. The period of time within a single cycle would be considered to be the "scan aperture."

Spiral CT, A method whereby projection images are gathered as the patient is moved through the scanning plane.

Tesla, A measure of magnetic flux per square meter

Volumetric, the acquisition of a stack of cross sectional images with near isotropic voxels.

Voxel, An image volume element. The two dimensional equivalent is a pixel. The term voxel recognizes that a cross sectional image has a thickness. A voxel is a three-dimensional point in space for which there is a reconstructed value (in the case of CT this is the x-ray attenuation coefficient or Hounsfield unit, in MRI the value can represent many different units of measure).

Z-axis, The axis running perpendicular to the scanned plane, typically head to foot in a recumbent patient.

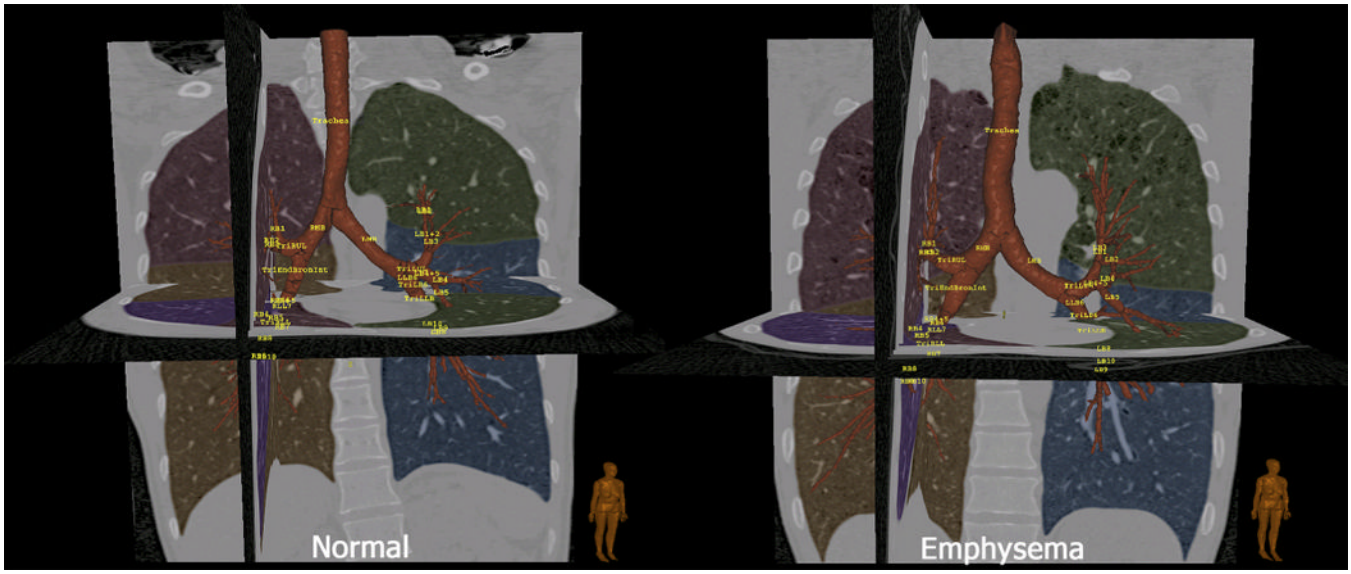

Figure 1.
Images derived from MDCT-based imaging of a normal non-smoker (left) and a smoker with emphysema (right). These images demonstrate the automatic segmentation of the lungs, lobes and bronchial tree with automatic bronchial tree labeling. Segmentation and display was via a Pulmonary Workstation Plus (VIDA Diagnostics: Coralville, Iowa)

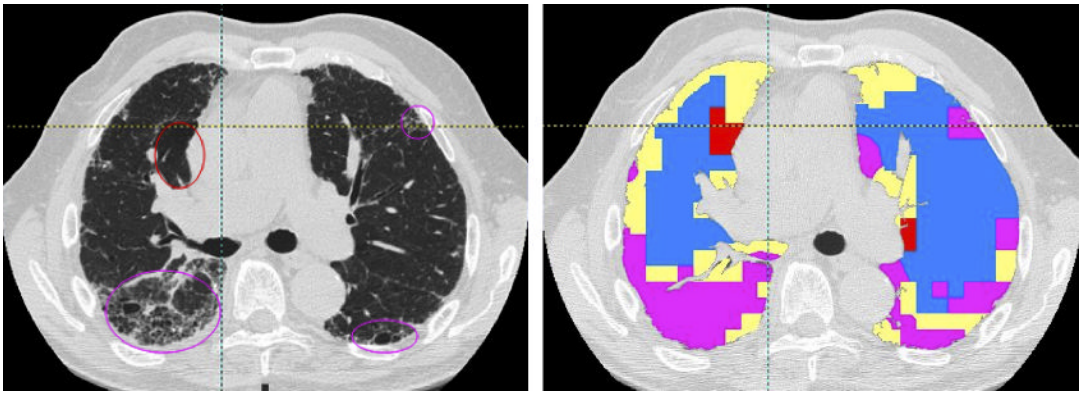

Figure 2.
Whole lung classification using the 3D AMFM. Ellipses in the original image slice (left) represent emphysema (red) and honeycomb (purple) patterns. The tissue types are color coded as: Red=emphysema, pink=honeycomb, blue=normal, and yellow=ground glass. (Data are from the thesis work of Ye Xu, University of Iowa, 2007)

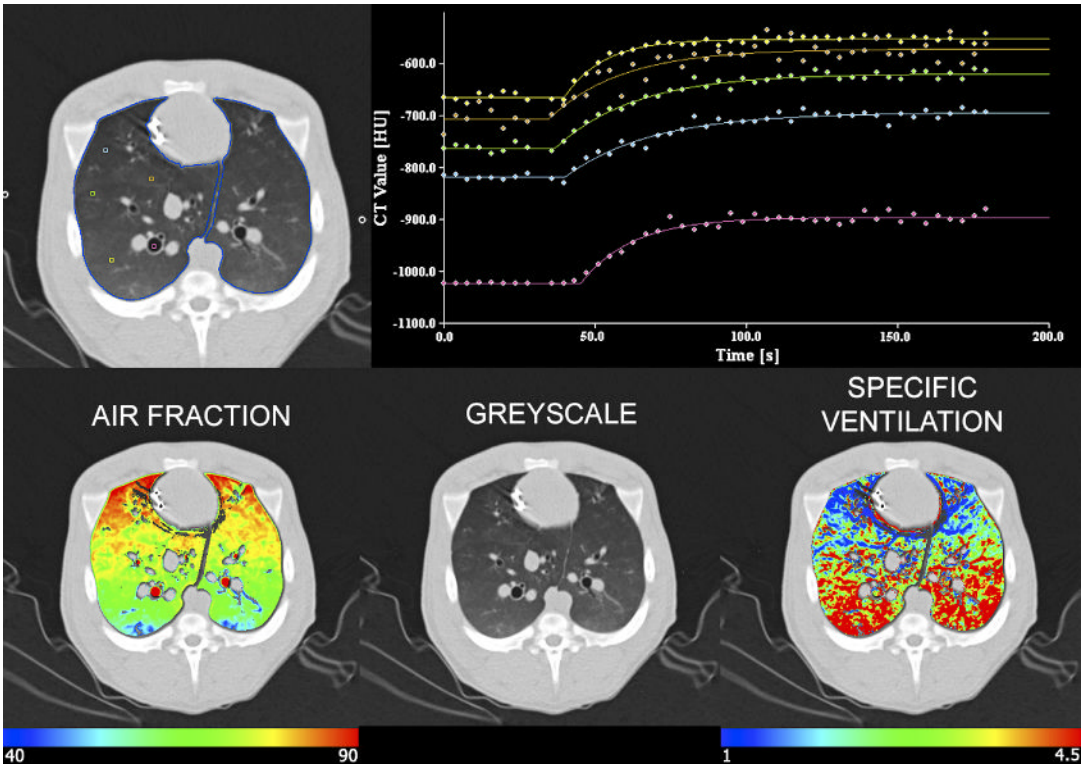

Figure 3.

Demonstration of the density changes occurring regionally across time as a result of the re-breathing of a constant concentration of xenon gas. Imaging is in the axial mode and scans are gated to end expiration. Data shown are from a supine anesthetized pig. In the upper panel, regions of interest are sampled including parenchymal regions spaced from the dependent to the non-dependent lung regions, with one region of interest in a right sided bronchus. It can be seen that the exponential rise from baseline is sharper in the dependent (yellow) region vs a much shallower exponential rise in the non-dependent region (blue). The sharp and shallow rise from baseline represent a fast or slow gas turnover rate respectively. Note the gradient in specific ventilation (lower right) where specific ventilation is the gas turn over rate (time constant) normalized by the local amount of air in that region of lung.

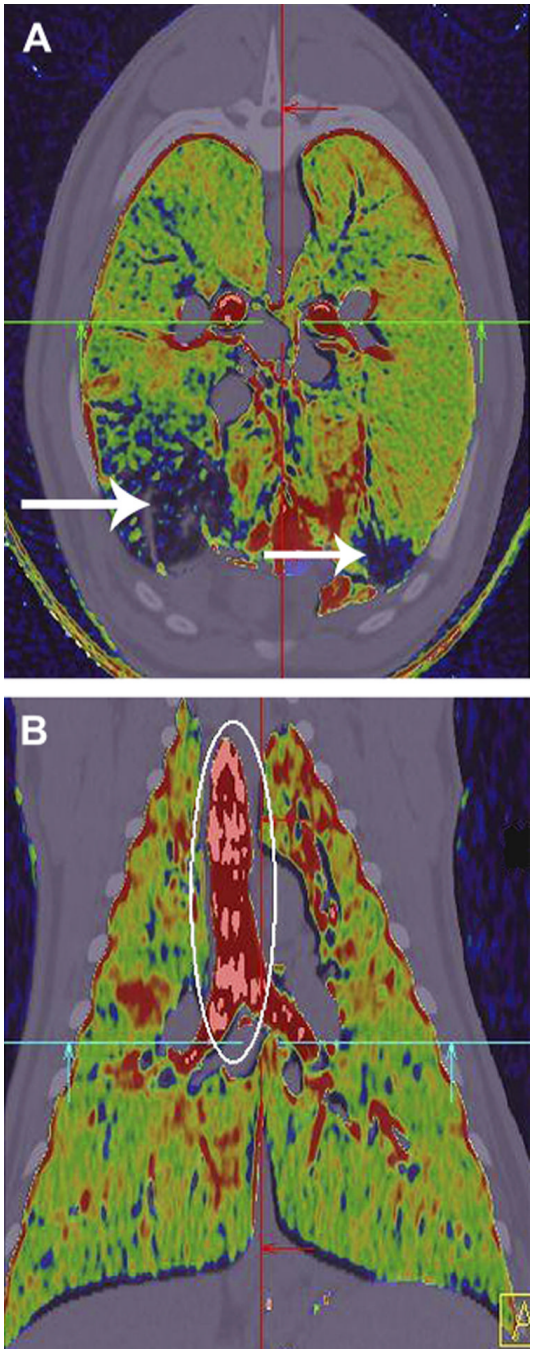

Figure 4.
Dual energy color coded images in axial (a) and coronal (b) planes demonstrate the presence of xenon gas following the inhalation of a single breath of 80% xenon. Imaging was accomplished in the prone position at 80 and 140kV, allowing subtraction of the xenon signal while minimally changing the signal from the natural occurring tissue of the body. Note the region of low or no xenon ventilation (white arrows, upper panel). This region had a ground glass pattern indicative of regional small airway inflammation. Data from the work of Fuld et al. [56] and Saba et al. [145]

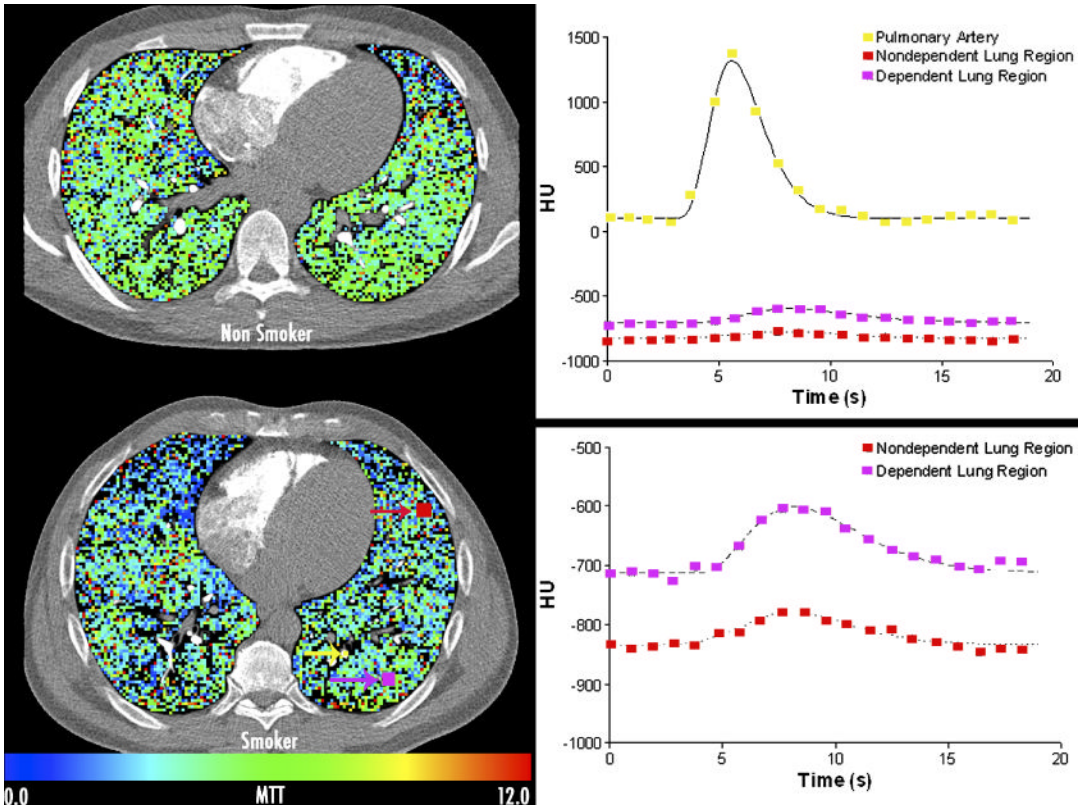

Figure 5.

Regional assessment of pulmonary blood flow mean transit times via use of temporally sequenced axial imaging, gated to the electrocardiogram during a sharp bolus contrast injection (0.5cc/kg iodinated contrast agent) into the superior vena cava / right atrial junction in a normal non-smoking (upper left) and a smoker (lower left) with CT showing only findings of early emphysema. Regions of interest are highlighted in the lower left image showing an ROI placed in the pulmonary artery (yellow); non-dependent (red) and dependent (purple) parenchymal regions. Associated time intensity curves are shown, from which mean transit times and pulmonary blood flow may be calculated, with the parenchymal curves expanded in the lower right graph. Studies have shown that the regional heterogeneity of pulmonary blood flow mean transit times are significantly increased in the smokers with CT findings of emphysema. Data from the work of Alford et al [3]

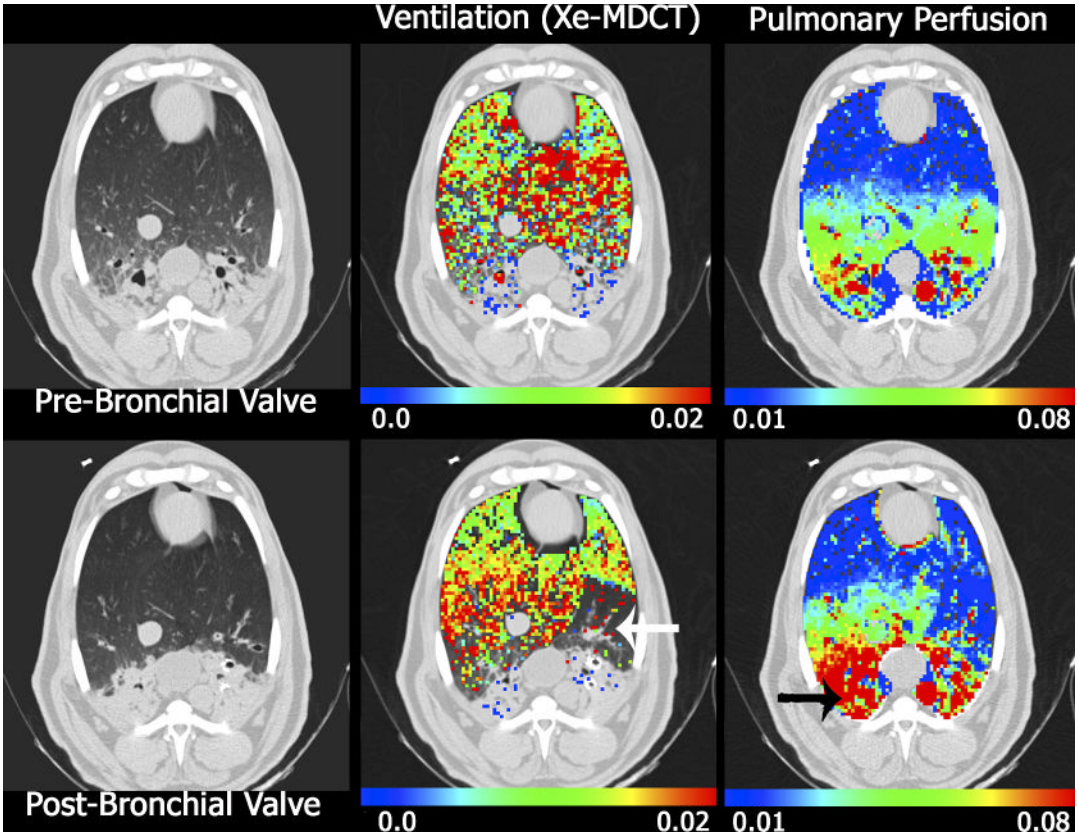

Figure 6.

Axial images from a sheep with native pneumonia (dependent lung regions), imaged supine, anesthetized in the MDCT scanner. Ventilation (middle column) and perfusion (left column) data sets were obtained before (upper rows) and after (lower rows) the placement of an endobronchial valve. The white arrow in the lower middle column marks the location of ventilation defect caused by the endobronchial valve. In this same region on the perfusion images (see lower right) there is a regional reduction in perfusion indicating regional, intact hypoxic pulmonary vasoconstriction. The black arrow in the lower right image marks a region that preferentially receives an increase in blood flow following the shunting of perfusion from the regional of the endobronchial valve, presumable because regional HPV is blocked in the presence of inflammation. Reprinted with permission from [74]

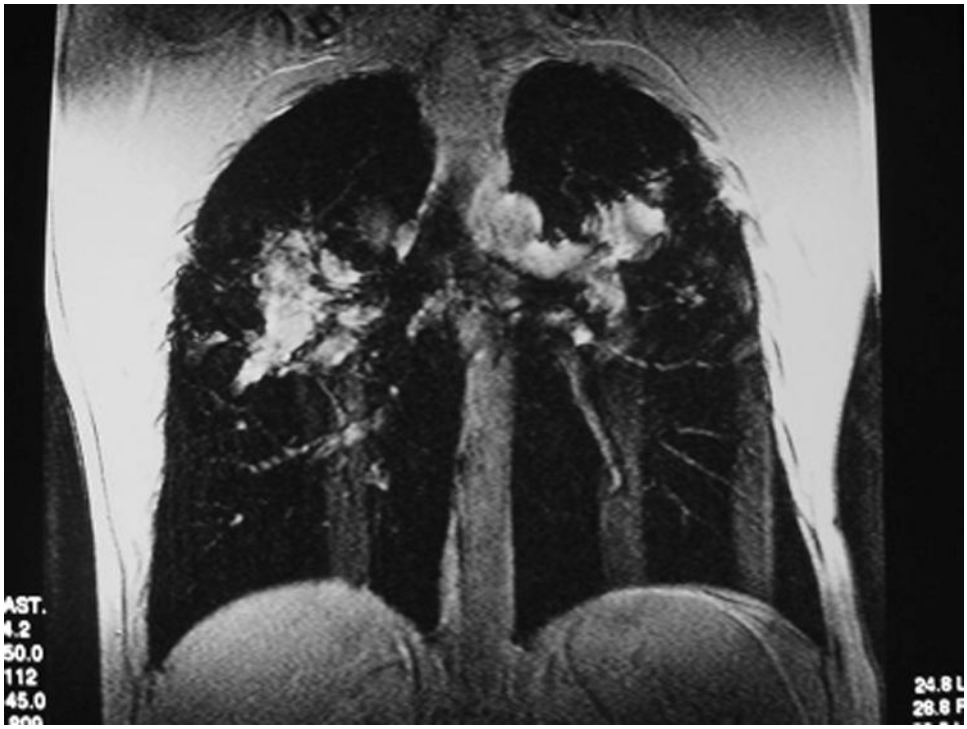

Figure 7.
Patient with sarcoidosis. Coronal proton single shot fast spin echo sequence, demonstrating black lungs with some interstitial markings and extensive mediastinal and bilateral hilar lymphadenopathy.

Figure 8.
Sagittal 3D-Gadolinium-enhanced MR angiogram, demonstrating direct connection between aorta and pulmonary artery (arrow), consistent with patent ductus arteriosus in a patient with pulmonary hypertension.

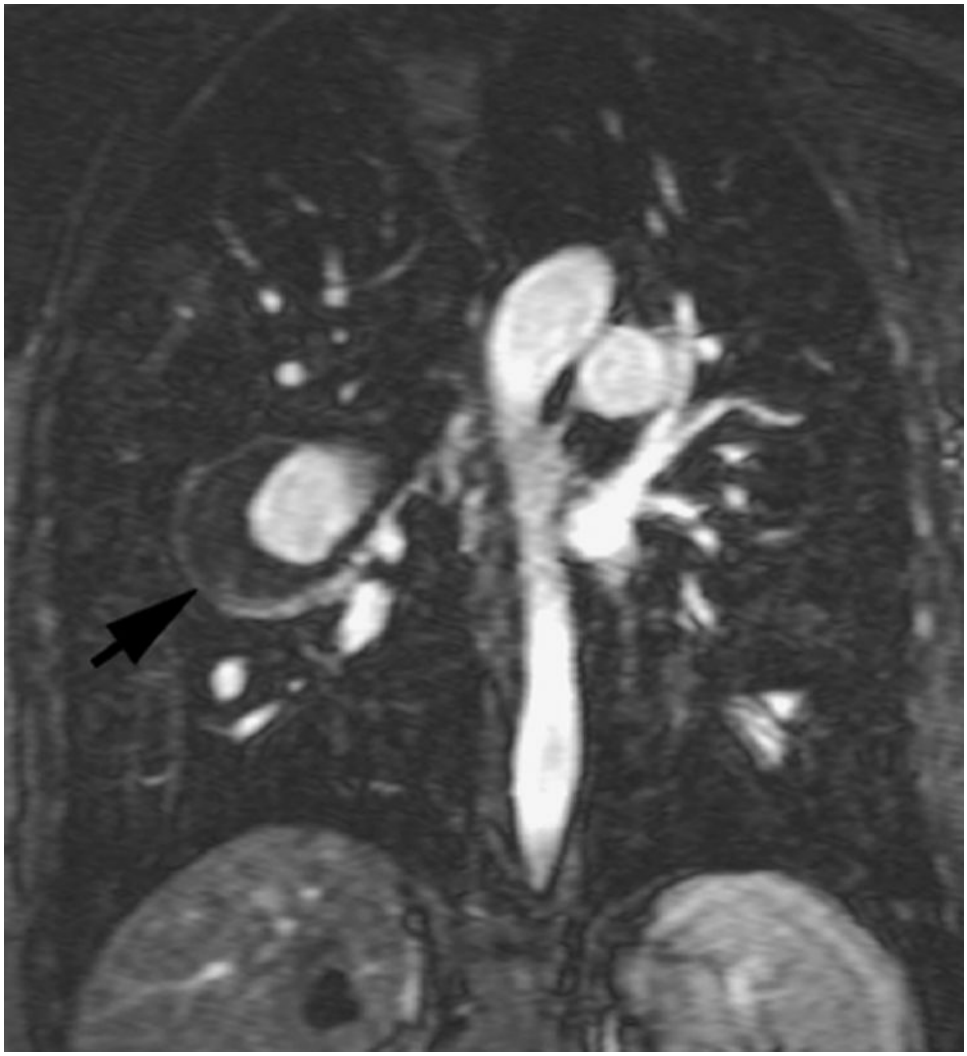

Figure 9.
Coronal 3D-Gadolinium-enhanced MR angiogram, demonstrating enhancement of an aneurysm of the right pulmonary artery with a black rim of mural organized thrombus (arrow) in a patient with pulmonary hypertension.

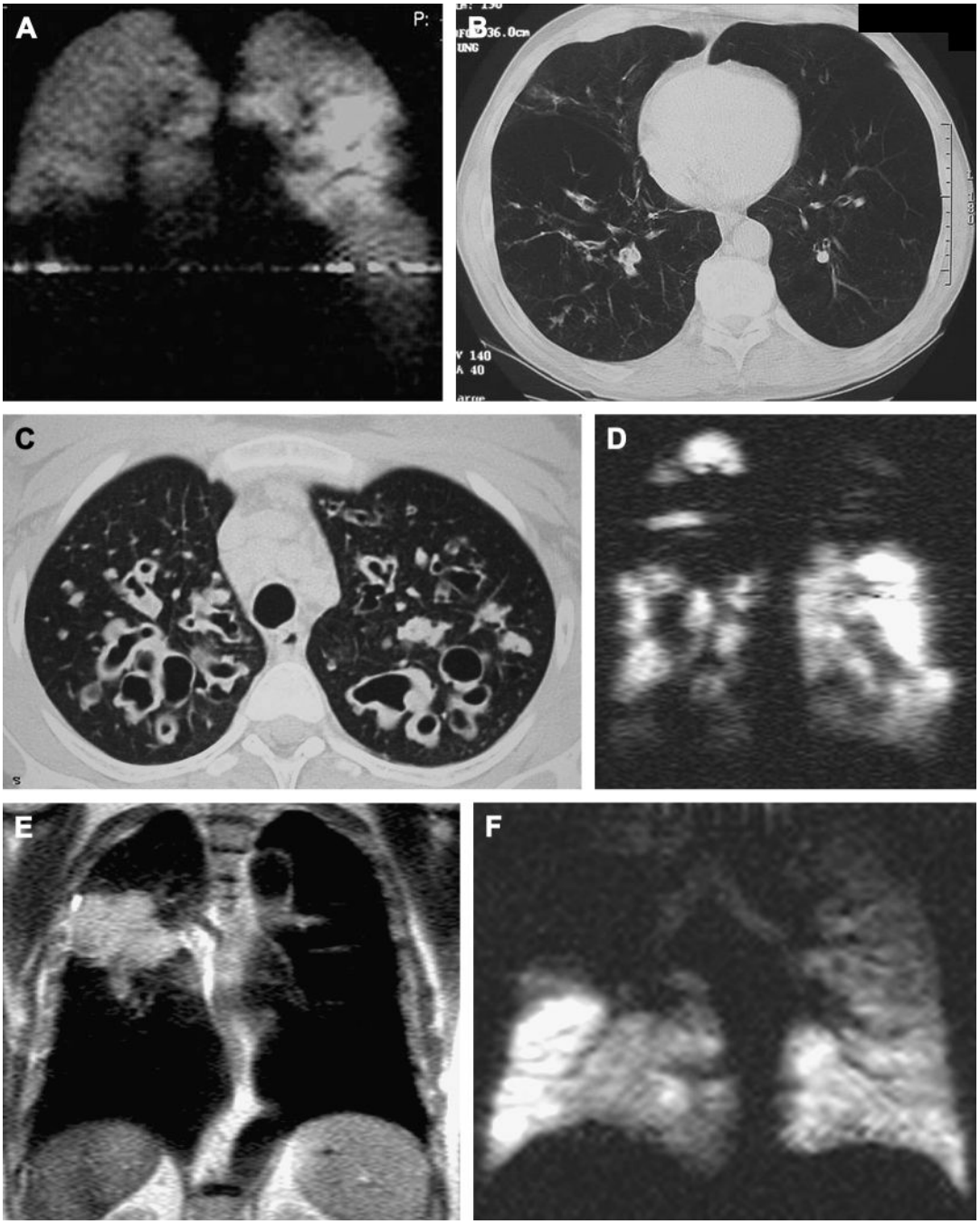

Figure 10.
Examples of hyperpolarized 3-Helium MRI and correlation with HRCT. A, B Patient with alpha-1-antitrypsin deficiency. Notice basal ventilation defects on coronal MRI (a), with corresponding panlobular emphysema on axial CT (b). C, D Patient with cystic fibrosis. Notice upper lobe cystic bronchiectasis on axial HRCT (C) with corresponding ventilation defects on coronal hyperpolarized 3-He MRI (D). E,F Patient with lung cancer. On coronal proton image a large soft tissue mass is visualized in the right upper lung(E), which corresponds to upper lobe ventilation defect on hyperpolarized 3-He MRI (F).

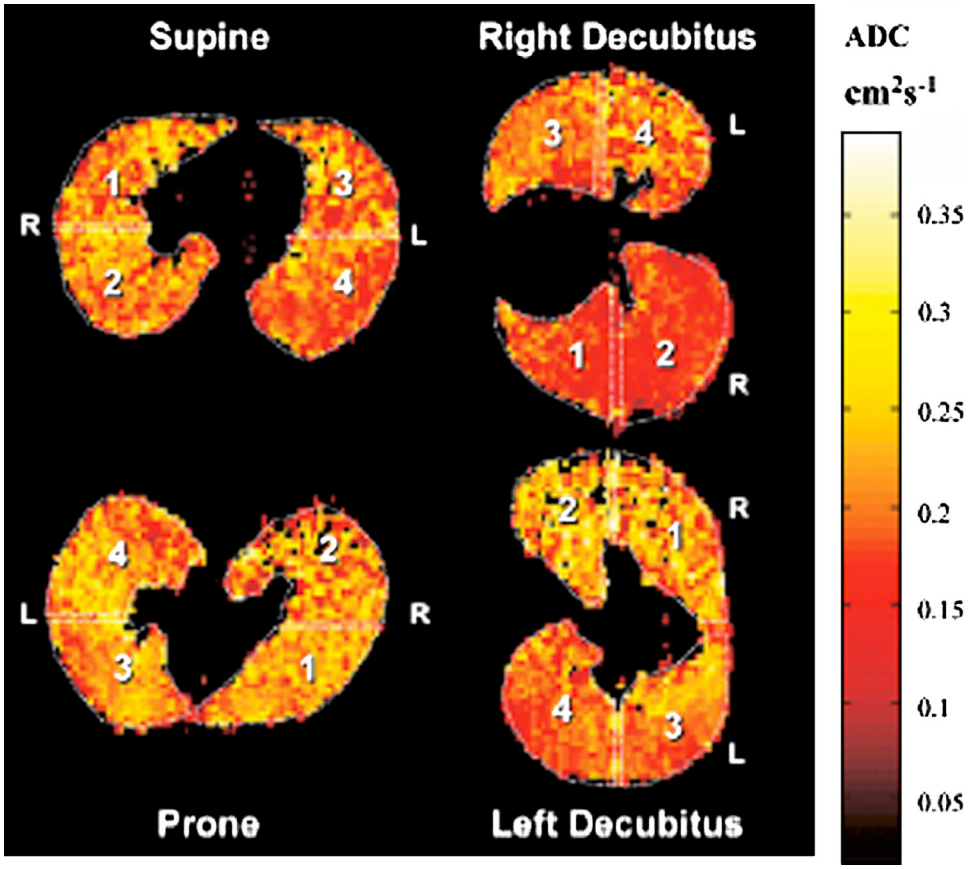

Figure 11.
Apparent diffusion coefficient (ADC) imaging in a normal volunteer in different positions, demonstrating gravity dependent changes with decreased ADC values in dependent lung portions (reproduced from Fichele et al. J MRI 2004;20:331–335.)

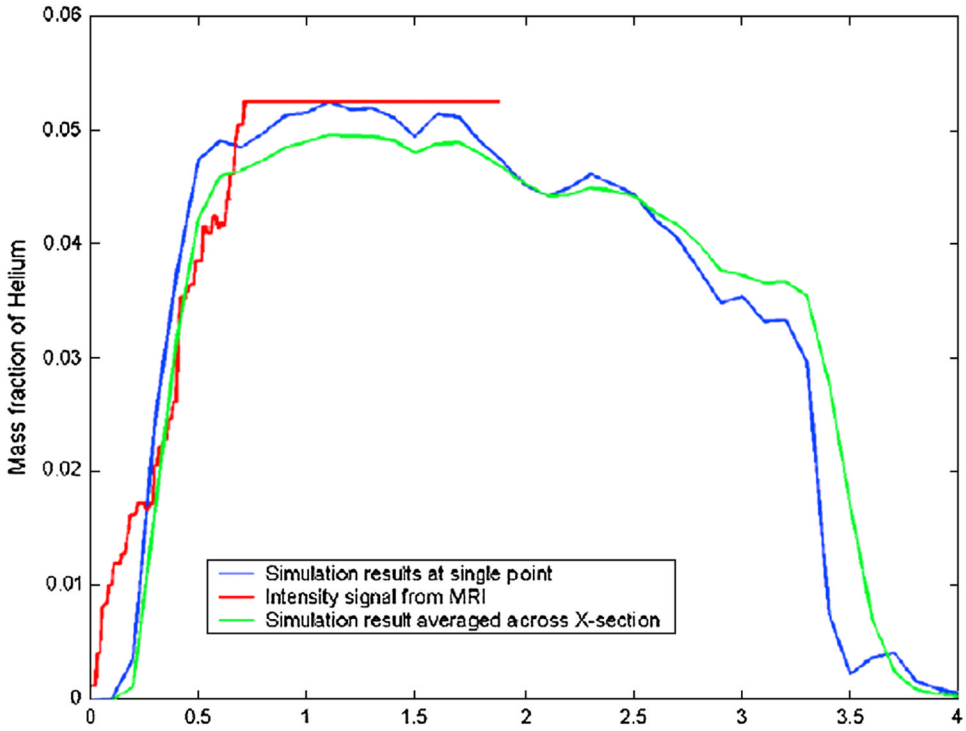

Figure 12.
Dynamic 3-He MRI reconstruction of signal change over time during single inspiration demonstrates the slope of the curve, which may be translated to forced inspiratory volume during 1 second (reproduced from Koumellis et al. J MRI 200522:420–426.)